



Pore-scale simulation of liquid CO₂ displacement of water using a two-phase lattice Boltzmann model



Haihu Liu ^{a,b,*}, Albert J. Valocchi ^a, Charles Werth ^a, Qinjun Kang ^c, Mart Oostrom ^d

^a Department of Civil & Environmental Engineering, University of Illinois at Urbana-Champaign, Urbana, IL 61801, USA

^b Department of Mechanical & Aerospace Engineering, University of Strathclyde, Glasgow G1 1XJ, UK

^c Earth and Environmental Sciences Division, Los Alamos National Laboratory, Los Alamos, NM 87545, USA

^d Hydrology Technical Group, Energy and Environment Division, Pacific Northwest National Laboratory, Richland, WA 99352, USA

ARTICLE INFO

Article history:

Received 29 October 2013

Received in revised form 23 April 2014

Accepted 29 July 2014

Available online 7 August 2014

Keywords:

Pore-scale simulation

Lattice Boltzmann model

Porous media

Multiphase flow

Fingering

Heterogeneity

ABSTRACT

A lattice Boltzmann color-fluid model, which was recently proposed by Liu et al. (2012) based on a concept of continuum surface force, is improved to simulate immiscible two-phase flows in porous media. The new improvements allow the model to account for different kinematic viscosities of both fluids and to model fluid-solid interactions. The capability and accuracy of this model is first validated by two benchmark tests: a layered two-phase flow with a variable viscosity ratio, and a dynamic capillary intrusion. This model is then used to simulate liquid CO₂ (LCO₂) displacing water in a dual-permeability pore network. The extent and behavior of LCO₂ preferential flow (i.e., fingering) is found to depend on the capillary number (*Ca*), and three different displacement patterns observed in previous micromodel experiments are reproduced. The predicted variation of LCO₂ saturation with *Ca*, as well as variation of specific interfacial length with LCO₂ saturation, are both in reasonable agreement with the experimental observations. To understand the effect of heterogeneity on pore-scale displacement, we also simulate LCO₂ displacing water in a randomly heterogeneous pore network, which has the same size and porosity as the simulated dual-permeability pore network. In comparison to the dual-permeability case, the transition from capillary fingering to viscous fingering occurs at a higher *Ca*, and LCO₂ saturation is higher at low *Ca* but lower at high *Ca*. In either pore network, the LCO₂-water specific interfacial length is found to obey a power-law dependence on LCO₂ saturation.

© 2014 Elsevier Ltd. All rights reserved.

1. Introduction

Carbon-based fuels, e.g., coal, oil and natural gas, are the backbone of the world economy until alternative energy systems mature. The best scientific evidence shows that the environment cannot sustain CO₂ emissions from carbon-based fuels without significant global warming. A promising approach for avoiding this impending crisis is to capture CO₂ from power plants and inject it into the deep subsurface for long-term sequestration [1,2]. Deep saline aquifers are considered the most likely candidate reservoirs for sequestering CO₂ because they are widely present, have a large capacity for storage, and are not used for water supply. When CO₂ is injected into deep saline aquifers, it exists in the liquid or supercritical state and displaces the formation fluid from the pore space in a complex pattern dictated by capillary and viscous forces, as

well as by large and small scale geological heterogeneities [3–5]. The dynamics of the displacement process determines the distribution of the injected CO₂ within the reservoir, which is one of the key parameters influencing CO₂ storage in terms of storage capacity, security and the ultimate fate of injected CO₂. It is, therefore, of great importance to study and understand the dynamic displacement process of CO₂ injection in porous media.

High-pressure visualization experiments of CO₂ injection provide a very useful tool to characterize and investigate the phase distributions and pore-scale mechanisms taking place during the displacement process [4,6–11]. Numerical simulations can complement experimental studies, opening an efficient pathway to an in-depth understanding of the effect of flow and physical parameters in the complicated three-dimensional (3D) porous media, thereby maximizing the benefit of a CO₂ injection process. However, numerical methods based on continuum description are insufficient for describing the influence of pore-scale parameters on macroscopic bulk properties [6]. Thus, the details of pore-scale flow patterns in the porous media cannot be resolved.

* Corresponding author at: Department of Civil & Environmental Engineering, University of Illinois at Urbana-Champaign, Urbana, IL 61801, USA.

E-mail address: haihliu@gmail.com (H. Liu).

Several approaches have been developed for pore-scale simulation of multiphase flows in porous media, including pore-network (PN) models [12–17], the lattice Boltzmann (LB) method [18–23], the smoothed particle hydrodynamics (SPH) method ([24–27]), and grid-based computational fluid dynamics (CFD) methods such as the volume-of-fluid (VOF) [28–30] and level-set (LS) methods [31,32]. PN models are a viable tool for understanding multiphase flows at the pore scale, and they are computationally efficient. These models, however, are based upon simplified representations of complex pore geometry and physics, which restricts their predictive capability and accuracy. The VOF method and the LS method simulate multiphase flows by solving the macroscopic Navier–Stokes equations (NSEs) together with a proper technique to track/capture the phase interface. It is challenging to use VOF and LS methods for pore-scale simulation of multiphase flows in porous media because of numerical instability arising at the interface region when the interfacial tension becomes a dominant factor [33]. Also, a suitable slip model with slip length at the molecular scale has to be introduced to avoid stress singularities at the moving contact line [29,30]. Microscopically, the interface between different phases and the contact-line dynamics on the solid surface are due to interparticle forces/interactions. Thus, mesoscopic level models are expected to describe accurately the interfacial dynamics in porous media. The SPH, which is a mesh-free Lagrangian particle method, does not need complex interface tracking schemes, and maintains a sharp interface free of numerical dispersion. Its similarity to the molecular dynamics simulations makes it easier to model fluid–fluid and fluid–surface interactions using interparticle forces. Nevertheless, the traditional SPH generally suffers from low accuracy, tensile instability, and difficulty in enforcing essential boundary condition [34].

In contrast, the LB method, as a mesoscopic numerical method, has been developed into a promising alternative to traditional CFD methods for simulating complex fluid flows [35–39] in recent years. The LB method has several advantages over the traditional CFD methods such as the ability to be programmed on parallel computers and the ease of dealing with complex boundaries [40]. Also, its kinetic nature provides many of the advantages of molecular dynamics, making the LB method well suited for pore-scale simulation of multiphase flows in complicated porous media. Currently, the most used multiphase LB models include the color-fluid model [41,42], the interparticle-potential model [43–45], the free-energy model [46,47] and the mean-field theory model [48]. Among these models, the interparticle-potential model was used extensively for two-phase flow problems in porous media, including capillary pressure hysteresis [18,21,49] and relative permeability [19,50–52]. However, the inter-particle potential model suffers from some limitations, including large spurious velocities in the vicinity of the fluid–fluid interface, viscosity-dependent equilibrium density and interfacial tension, and numerical instability for large viscosity or density ratios. For example, the kinematic viscosity ratio is typically restricted to no more than 5 [53]. There have been ongoing efforts to alleviate these limitations [54–56], but their effectiveness in dealing with multiphase flow in complex porous media has not been fully investigated. For a comprehensive review of multiphase LB models, interested readers may refer to Refs. [35,40,57].

In this work, we extend our recently developed LB color-fluid model [58] for simulating two-phase flows in porous media. The extensions include an improvement for handling immiscible binary fluids with different kinematic viscosities and the capability of modeling fluid–surface interactions, i.e., contact-line dynamics on a solid surface, in a simple way. The usefulness and accuracy of this model is first examined by two test cases with theoretical solutions. This model is then used to simulate LCO₂ displacement of water in a dual-permeability pore network, comparing the

simulation results with previous micromodel experiments described in Zhang et al. [9]. Finally, we simulate LCO₂ displacement of water in a randomly heterogeneous pore network because (1) geological formations are natural heterogeneous porous media with varying pore size, permeability and porosity and (2) several laboratory studies [59–62] have revealed the significant effect of media heterogeneity on steady-state migration patterns, phase distributions, and CO₂ saturation. We compare the obtained results with those in the dual-permeability pore network, uncovering the impact of heterogeneity on drainage behavior. This study improves our understanding of unstable displacement processes involved in the geological carbon storage.

2. Methodology

The model we use in the LB simulations is an immiscible two-phase lattice Bhatnagar–Gross–Krook (BGK) algorithm, where we introduce capillary force and phase segregation following the method of Liu et al. [58]. In this model, red and blue distribution functions f_i^R and f_i^B are used to represent two different fluids, and the total distribution function is defined as: $f_i = f_i^R + f_i^B$. Each of the colored fluids undergoes the collision and streaming operations

$$f_i^k(\mathbf{x} + \mathbf{e}_i \delta_t, t + \delta_t) = f_i^k(\mathbf{x}, t) + \Omega_i^k(\mathbf{x}, t), \quad (1)$$

where the superscript $k = R$ or B denotes the color (“Red” or “Blue”), $f_i(\mathbf{x}, t)$ is the distribution function in the i th velocity direction at position \mathbf{x} and time t , \mathbf{e}_i is the lattice velocity in the i th direction, δ_t is the time step, and Ω_i^k is the collision operator. The collision operator is the result of the combination of three sub-operators:

$$\Omega_i^k = (\Omega_i^k)^{(3)} \left[(\Omega_i^k)^{(1)} + (\Omega_i^k)^{(2)} \right], \quad (2)$$

where $(\Omega_i^k)^{(1)}$ is the single-phase collision operator, $(\Omega_i^k)^{(2)}$ is the perturbation operator which contributes to the mixed interfacial region and generates an interfacial tension, and $(\Omega_i^k)^{(3)}$ represents the recoloring operator which mimics the phase segregation and keeps the interface sharp.

Using the BGK approximation, the single-phase collision operator is given as

$$(\Omega_i^k)^{(1)} = -\frac{1}{\tau} (f_i^k - f_i^{k,eq}) + \Phi_i, \quad (3)$$

where τ is the dimensionless relaxation time, and $f_i^{k,eq}$ is the equilibrium distribution function of f_i^k . Conservation of mass for each fluid and total momentum conservation require

$$\rho_k = \sum_i f_i^k = \sum_i f_i^{k,eq}, \quad (4)$$

$$\rho \mathbf{u} = \sum_k \sum_i f_i^k \mathbf{e}_i = \sum_k \sum_i f_i^{k,eq} \mathbf{e}_i, \quad (5)$$

where ρ_k is the density of fluid k , $\rho = \rho_R + \rho_B$ is the total density and \mathbf{u} the local fluid velocity. For the two-dimensional 9-velocity (D2Q9) model [63], the lattice velocity \mathbf{e}_i is defined as $\mathbf{e}_0 = (0, 0)$, $\mathbf{e}_{1,3} = (\pm c, 0)$, $\mathbf{e}_{2,4} = (0, \pm c)$, $\mathbf{e}_{5,7} = (\pm c, \pm c)$, and $\mathbf{e}_{6,8} = (\mp c, \pm c)$, where $c = \delta_x / \delta_t$ is the lattice speed and δ_x the lattice spacing. In this study, both fluids are assumed to have equal density for the sake of simplicity, which is acceptable because gravity plays a negligible role in determining the displacement behavior in micromodels compared with the capillary and viscous forces [64]. By satisfying the conservation constraints of Eqs. (4) and (5), a popular choice for the equilibrium distribution functions is

$$f_i^{k,eq} = \rho_k w_i \left[1 + \frac{3}{c^2} \mathbf{e}_i \cdot \mathbf{u} + \frac{9}{2c^4} (\mathbf{e}_i \cdot \mathbf{u})^2 - \frac{3}{2c^2} \mathbf{u}^2 \right], \quad (6)$$

where w_i is the weight factor with $w_0 = 4/9$, $w_{1-4} = 1/9$ and $w_{5-8} = 1/36$. Besides, an additional term Φ_i is introduced into Eq. (3) to account for the effect of body force \mathbf{G} . It can be simply given by $\Phi_i = \frac{3}{c^2} w_i \mathbf{e}_i \cdot \mathbf{G} \delta_t$ when the body force is a constant [65].

Liu et al. [58] recently derived a generalized perturbation operator for the three-dimensional 19-velocity (D3Q19) lattice based on the concept of a continuum surface force (CSF) along with the constraints of mass and momentum conservation. In a similar way, a generalized perturbation operator can be derived for D2Q9 lattice, i.e.,

$$(\Omega_i^{(2)})^{(2)} = \frac{A_k}{2} |\nabla \rho^N| \left[w_i \frac{(\mathbf{e}_i \cdot \nabla \rho^N)^2}{|\nabla \rho^N|^2} - B_i \right], \quad (7)$$

where the phase field ρ^N is defined as

$$\rho^N(\mathbf{x}, t) = \frac{\rho_R(\mathbf{x}, t) - \rho_B(\mathbf{x}, t)}{\rho_R(\mathbf{x}, t) + \rho_B(\mathbf{x}, t)}, \quad -1 \leq \rho^N \leq 1 \quad (8)$$

and

$$B_0 = -\frac{\chi}{3\chi + 6} c^2, \quad B_{1-4} = \frac{\chi}{6\chi + 12} c^2, \quad B_{5-8} = \frac{1}{6\chi + 12} c^2. \quad (9)$$

In the above equation, χ is a free parameter, which is taken as $\chi = 4$ in this study. In addition, an expression for interfacial tension (σ) can be analytically obtained without any additional analysis or assumptions as done in Refs. [42,66,67]

$$\sigma = \frac{2}{9} A \tau c^4 \delta_t, \quad (10)$$

where $A = \sum_k A_k$. Eq. (10) suggests that the interfacial tension can be flexibly chosen by adjusting A . Its validity was demonstrated by stationary bubble tests, see Ref. [58].

Employing the Chapman–Enskog multiscale analysis, Eq. (1) can be reduced to the NSEs in the low frequency, long wavelength limit with Eqs. (3), (6), (7) and (10). The resulting equations are [58]

$$\partial_t \rho + \nabla \cdot (\rho \mathbf{u}) = 0, \quad (11)$$

$$\partial_t(\rho \mathbf{u}) + \nabla \cdot (\rho \mathbf{u} \mathbf{u}) = -\nabla p + \nabla \cdot [\eta(\nabla \mathbf{u} + \nabla \mathbf{u}^T)] + \mathbf{F}_S, \quad (12)$$

where $p = \frac{1}{3} \rho c^2$ is the pressure, $\eta = \frac{1}{3} \rho c^2 (\tau - \frac{1}{2}) \delta_t$ is the dynamic viscosity of the fluid mixture, and \mathbf{F}_S is a volume-distributed interfacial force and is given by [58]

$$\mathbf{F}_S = \nabla \cdot [\sigma(\mathbf{I} - \mathbf{n} \otimes \mathbf{n}) \delta_\Sigma]. \quad (13)$$

Here, $\mathbf{n} = \frac{\nabla \rho^N}{|\nabla \rho^N|}$ is the unit vector normal to the interface, $\delta_\Sigma = \frac{1}{2} |\nabla \rho^N|$ is the Dirac delta function, and \mathbf{I} the second-order identity tensor. Note that Eq. (13) has been extensively used to model the capillary force in VOF and LS methods.

It will be shown shortly that the total distribution function is only required in order to perform the subsequent recoloring operation. Therefore, it is not necessary to calculate both the single-phase collision (Eq. (3)) and perturbation step (Eq. (7)) separately for each fluid. With the total distribution function f_i , the single-phase collision and perturbation operators can be expressed as

$$(\Omega_i^{(1)})^{(1)} = -\frac{1}{\tau} (f_i - f_i^{eq}) + \Phi_i \quad (14)$$

and

$$(\Omega_i^{(2)})^{(2)} = \frac{A}{2} |\nabla \rho^N| \left[w_i \frac{(\mathbf{e}_i \cdot \nabla \rho^N)^2}{|\nabla \rho^N|^2} - B_i \right], \quad (15)$$

respectively, where $f_i^{eq} = \sum_k f_i^{k,eq}$. Since the multiple-relaxation-time (MRT) scheme is advantageous over the BGK approximation in enhancing numerical stability [55,68] and suppressing spurious velocities at the phase interface [69–71], it has been widely used for simulating multiphase/multicomponent flows instead of the

BGK approximation. With the MRT scheme, the collision operator $(\Omega_i^{(1)})^{(1)}$ is given by

$$(\Omega_i^{(1)})^{(1)} = -\left(\mathbf{M}^{-1} \mathbf{S} \mathbf{M} \right)_{ij} (f_j - f_j^{eq}) + \Phi_i, \quad (16)$$

where \mathbf{M} is a transformation matrix [71], which is designed to contain more physically relevant quantities, e.g. density, momentum, energy, and their fluxes. \mathbf{S} is a diagonal relaxation matrix defined by

$$\mathbf{S} = \text{diag}[s_0, s_1, s_2, s_3, s_4, s_5, s_6, s_7, s_8], \quad (17)$$

where the elements s_i are the relaxation rates associated with each f_i . The parameters s_0 , s_3 and s_5 correspond to the conserved moments (i.e., density and momentum) and are chosen as $s_0 = s_3 = s_5 = 0$. s_7 and s_8 are related to τ by $s_7 = s_8 = \frac{1}{\tau}$. Besides, symmetry requires that $s_4 = s_6$. As a result, three independent parameters s_1 , s_2 and s_4 ($= s_6$) can be freely adjusted to enhance the stability of the model and minimize spurious velocities at the phase interface. Note that the MRT scheme will reduce to the BGK approximation if all s_i in Eq. (17) are set to $1/\tau$.

To account for unequal viscosities of the two fluids, a harmonic mean is used to determine the viscosity of the fluid mixture [72]

$$\frac{1}{\eta} = \frac{1 + \rho^N}{2\eta_R} + \frac{1 - \rho^N}{2\eta_B} \quad \text{or} \quad \frac{1}{\tau - 0.5} = \frac{1 + \rho^N}{2(\tau_R - 0.5)} + \frac{1 - \rho^N}{2(\tau_B - 0.5)}, \quad (18)$$

where η_k ($k = R$ or B) is the dynamic viscosity of fluid k , which is related to the dimensionless relaxation time τ_k as $\eta_k = \frac{1}{3} \rho_k c^2 (\tau_k - \frac{1}{2}) \delta_t$. In the present diffuse-interface model, the choice of Eq. (18) can ensure a constant viscosity flux across the interface, which can be explained as follows. Consider a horizontal interface in the x - y plane that separates the red and blue fluids on both sides. The viscosity flux is written by $\eta \partial_y u_x$ [73], which should be a constant across the interface based on a force balance. This will imply that the velocity gradient $\partial_y u_x$ is not a constant across the interface when both fluids have different viscosities. We define $(\partial_y u_x)_R$ and $(\partial_y u_x)_B$ as the velocity gradients on the red and blue fluid sides, respectively. Also, we simply take the velocity gradient at the interface as $\frac{1+\rho^N}{2} (\partial_y u_x)_R + \frac{1-\rho^N}{2} (\partial_y u_x)_B$ by assuming that the velocity gradient varies linearly with ρ^N . A constant viscosity flux across the interface requires $\eta \left[\frac{1+\rho^N}{2} (\partial_y u_x)_R + \frac{1-\rho^N}{2} (\partial_y u_x)_B \right] = \eta_R (\partial_y u_x)_R = \eta_B (\partial_y u_x)_B$, which can easily lead to Eq. (18). We note that the harmonic mean was also used for the interface viscosity to ensure the continuity of viscosity flux in the sharp-interface models [66,74]. Our simulation results will also demonstrate that this form of function for τ (or τ) behaves better than other popular choices in the LB color-fluid models, which read [75–78]

$$\tau = \frac{1 + \rho^N}{2} \tau_R + \frac{1 - \rho^N}{2} \tau_B, \quad (19)$$

$$\frac{1}{\tau} = \frac{1 + \rho^N}{2} \frac{1}{\tau_R} + \frac{1 - \rho^N}{2} \frac{1}{\tau_B}. \quad (20)$$

Note that several other interpolation schemes have also been constructed to account for different viscosities in the color-fluid models, see Refs. [42,79].

The calculation of partial derivatives is required to evaluate the local gradient of the phase field. To minimize the discretization error, these derivatives are calculated using 9-point finite difference stencils as follows [58]:

$$\frac{\partial \rho^N(\mathbf{x})}{\partial x_z} = \frac{3}{c^2} \sum_i w_i \rho^N(\mathbf{x} + \mathbf{e}_i \delta_t) e_{iz}. \quad (21)$$

Although the perturbation operator generates the interfacial tension, it does not guarantee the immiscibility of both fluids. To promote phase segregation and maintain the interface, the recoloring algorithm proposed by Latva-Kokko and Rothman [80]

is applied. This algorithm allows the red and blue fluids to mix moderately at the tangent of the interface, and at the same time keeps the color distribution symmetric with respect to the color gradient. Thus, it can help reduce the spurious currents and remove the lattice pinning problem produced by the original recoloring algorithm of Gunstensen et al. [81]. Following Latva-Kokko and Rothman [80], the recoloring operators for the red and blue fluids are defined by

$$(\Omega_i^R)^{(3)}(f_i^R) = \frac{\rho_R}{\rho} f_i^* + \beta \frac{\rho_R \rho_B}{\rho} w_i \cos(\varphi_i), \quad (22)$$

$$(\Omega_i^B)^{(3)}(f_i^B) = \frac{\rho_B}{\rho} f_i^* - \beta \frac{\rho_R \rho_B}{\rho} w_i \cos(\varphi_i), \quad (23)$$

where f_i^* denotes the post-perturbation, pre-segregation value of the total distribution function along i th lattice direction. β is the segregation parameter and is fixed at 0.7 to maintain a narrow interface thickness and reduce spurious currents [82]; several recent studies [58,76] also showed that this choice is necessary to reproduce correct interface dynamics. φ_i is the angle between the phase field gradient $\nabla \rho^N$ and the lattice vector \mathbf{e}_i , which is defined by

$$\cos(\varphi_i) = \frac{\mathbf{e}_i \cdot \nabla \rho^N}{|\mathbf{e}_i| |\nabla \rho^N|}. \quad (24)$$

The halfway bounce-back scheme [83] is applied at the solid walls to obtain no-slip condition. This scheme strictly conserves the mass of the fluid particles prior to and after the collision with the solid walls. Interactions between solid and fluids determine the wetting properties of a multiphase system, which are usually characterized by a static contact angle θ according to force balance at the three-phase contact line: $\sigma \cos(\theta) = \sigma_{Rs} - \sigma_{Bs}$, where σ_{Rs} (σ_{Bs}) is the interfacial tension between the red (blue) fluid and the solid surface. In the present model, we follow the assumption of Rowlinson and Widom [84] that the solid wall is a mixture of two fluids, thus having a certain value of the phase field ρ_s^N . The gradient of the phase field near the wall boundary can therefore be calculated using Eq. (21). Consequently, the interfacial force term, i.e., the perturbation operator in Eq. (7) becomes dependent on the properties of the neighboring solid lattice sites, resulting in a special case of the wetting boundary condition. Fig. 1 demonstrates that different contact angles can be obtained by adjusting the value of the phase field at the solid wall. In these simulations, the initial condition is a semicircular stationary droplet (red fluid) with radius $R = 25$ lattices sitting along the center line on the bottom wall, and the final steady states are shown in the figure. In the LB community, similar approaches were also adopted by Bekri and Adler [85] in the original model of Gunstensen et al., by van der Graaf et al. [86] and Liu and Zhang [87,88] in the free-energy models, by Martys and Chen [89] in the interparticle-potential model through the fluid–solid interaction potential, and by Yiotsis et al. [90] in the mean-field

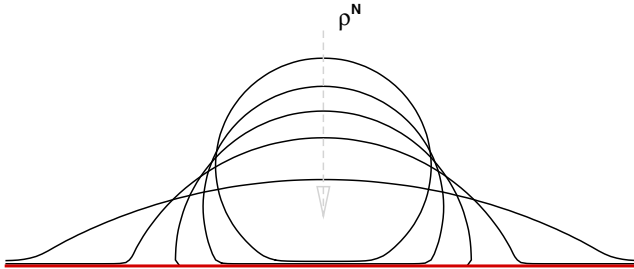


Fig. 1. Different contact angles obtained through adjusting the phase field ρ_s^N at the solid wall. The values of ρ_s^N are taken as $\rho_s^N = \{-0.8, -0.4, 0, 0.4, 0.8\}$ along the direction of arrow. The size of the computational domain is 200×100 lattice cells.

theory model. In addition, in the free-energy models, the contact angle can be modeled by a surface integral that appears in the boundary condition of the free energy [91,71].

3. Results and discussion

The section is organized as follows. Section 3.1 uses two benchmark cases to validate the developed color-fluid model, focusing on two important extensions. Sections 3.2 and 3.3 use the BGK color-fluid model to simulate immiscible two-phase displacement in a dual-permeability pore network and in a randomly heterogeneous pore network. The obtained results in the dual-permeability pore network are compared with a previously published micromodel experiment, and the simulation results in both pore networks are compared to show the effect of media heterogeneity. Finally, in Section 3.4 we demonstrate that the currently-used BGK color-fluid model can reasonably capture two-phase displacement behavior in porous media.

3.1. Model validation

The color-fluid model has been validated through the study of several droplet problems in Ref. [58]. Here two more validation cases are carried out to examine the major enhancements in the present work, including (1) the improvement to handle immiscible binary fluids with different viscosities, and (2) the capability of modeling fluid–surface interactions. For the first validation case, we consider immiscible layered two-phase flow between two infinite plates. As illustrated in Fig. 2, the channel height is $2b$ in the y direction with $y = 0$ at the center of the channel. Initially, the red fluid (non-wetting phase) is located in the central region $0 < |y| < a$, while the blue fluid (wetting phase) is located in the region $a < |y| < b$. The flow is driven by constant body forces in the x direction with different magnitudes G_R and G_B acting on the red and blue fluids, respectively. Both fluids have the same density and their kinematic viscosities are ν_R and ν_B . Assuming a Poiseuille-type flow in the channel, the analytical solution for the velocity profile $u_x(y)$ between the parallel plates can be obtained

$$u_x(y) = \begin{cases} A_1 y^2 + C_1 & (0 \leq |y| \leq a), \\ A_2 y^2 + B_2 y + C_2 & (a \leq |y| \leq b), \end{cases} \quad (25)$$

where the coefficients are given by

$$A_1 = -\frac{G_R}{2\nu_R}, \quad A_2 = -\frac{G_B}{2\nu_B}, \quad B_2 = 2(A_1 M - A_2)a, \quad (26)$$

$$C_1 = (A_2 - A_1)a^2 - B_2(b - a) - A_2 b^2, \quad C_2 = -A_2 b^2 - B_2 b \quad (27)$$

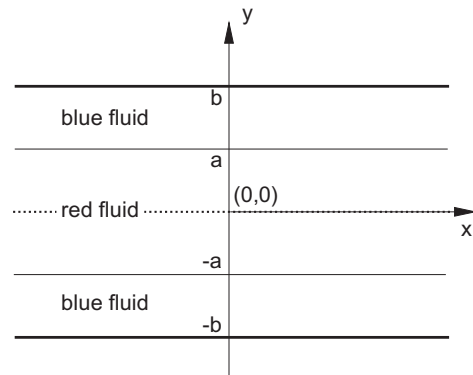


Fig. 2. Schematic of the layered two-phase flow between two parallel plates. The red (non-wetting) fluid flows in the central region $0 < |y| < a$, while the blue (wetting) fluid flows in the region $a < |y| < b$.

and $M = \frac{\nu_R}{\nu_B}$ is the viscosity ratio.

Simulations are conducted in a 10×200 lattice domain with the velocity initialized to zero everywhere. The periodic boundary condition is applied in the x direction and the no-slip boundary condition is imposed on the upper and lower walls. Four cases with different force magnitudes and distributions at different viscosity ratios are investigated: (a) $G_R = 1.5 \times 10^{-8}$, $G_B = 0$, $M = 0.08$; (b) $G_R = 1.5 \times 10^{-8}$, $G_B = 0$, $M = 12.5$; (c) $G_R = 0$, $G_B = 1.5 \times 10^{-8}$, $M = 0.08$; (d) $G_R = 0$, $G_B = 1.5 \times 10^{-8}$, $M = 12.5$. Other parameters are fixed as $a = \frac{b}{2} = 50$, $\rho_R = \rho_B = 1$, and $\sigma = 10^{-2}$. Fig. 3 compares the velocity profiles obtained through our simulations with τ determined by Eq. (18) to those given by Eq. (25) for the above four cases. The numerical results agree quite well with the analytical solutions for all cases. However, the numerical results will deviate from the analytical solutions when the relaxation time τ is determined by Eq. (19) or (20), which can be clearly seen in Fig. 4.

Capillary intrusion, which originated from the pioneering work of Washburn [92], provides a good benchmark for assessing whether a multiphase model is able to simulate moving contact line problems. The velocity of a wetting fluid column intruding a horizontal capillary tube, as shown in Fig. 5, is determined by the balance between the pressure difference over the interface, the Laplace pressure, and the viscous drag of the intruding fluid. If

the gravity and inertial effects are neglected, this balance can be expressed as [93,94]

$$\sigma \cos(\theta) = \frac{6}{r} [\eta_B x + \eta_R (L - x)] \frac{dx}{dt}, \quad (28)$$

where θ is the contact angle, r is the capillary tube width, x the position of the phase interface, and η_R and η_B are the dynamic viscosities of the red (non-wetting) and blue (wetting) fluids, respectively. In the analytical derivation, θ is specified as a wall boundary condition. However, for comparison with simulations or experiments, θ should be taken as the dynamic contact angle [93,94]. The system consists of a 600×25 lattice domain with periodic boundary conditions in the x direction. In the middle portion the boundaries of the capillary tube are no-slip and wetting. The length of the capillary tube is taken as $L = 300$ lattices. Outside of the middle portion, the boundary conditions are periodic in the y direction. We run the simulations with the parameters $\rho_R = \rho_B = 1$, $\sigma = 5 \times 10^{-3}$ and $r = 15$ for two different viscosity ratios: (a) $M = 1$ and (b) $M = 0.1$. We also choose $\rho_s^N = -0.71$ to represent hydrophilic capillary tube for the intruding blue fluid ($\rho^N = -1$). Fig. 6 shows the comparison between our simulation results and the analytical predictions from Eq. (28) for $M = 1$ and 0.1 . Note that Eq. (28) is plotted using the dynamic contact angle, measured from our LB simulations. It can

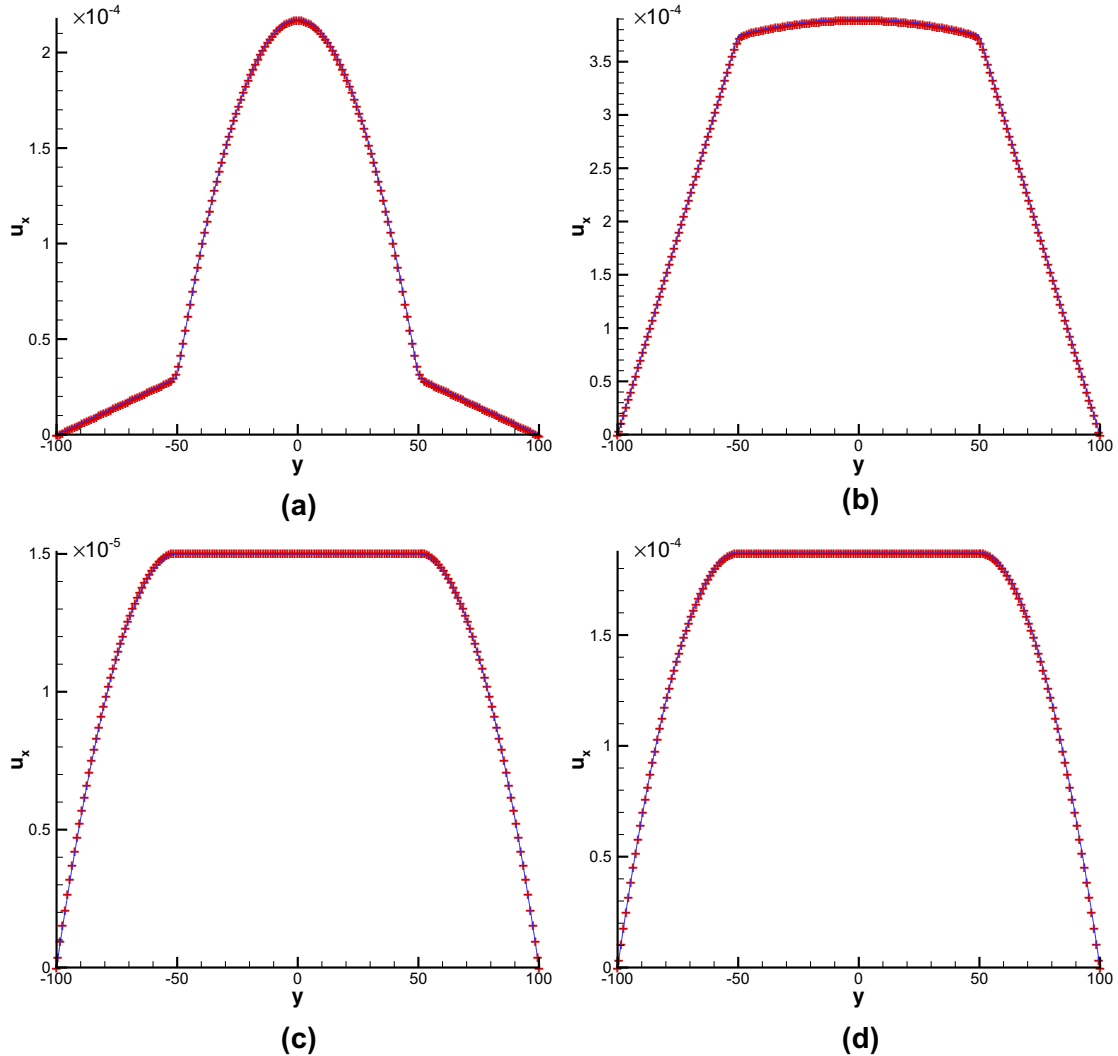


Fig. 3. Simulated (symbols) and analytical (lines) velocity profiles for layered two-phase flow under four different conditions: (a) $G_R = 1.5 \times 10^{-8}$, $G_B = 0$, $M = 0.08$; (b) $G_R = 1.5 \times 10^{-8}$, $G_B = 0$, $M = 12.5$; (c) $G_R = 0$, $G_B = 1.5 \times 10^{-8}$, $M = 0.08$; and (d) $G_R = 0$, $G_B = 1.5 \times 10^{-8}$, $M = 12.5$.

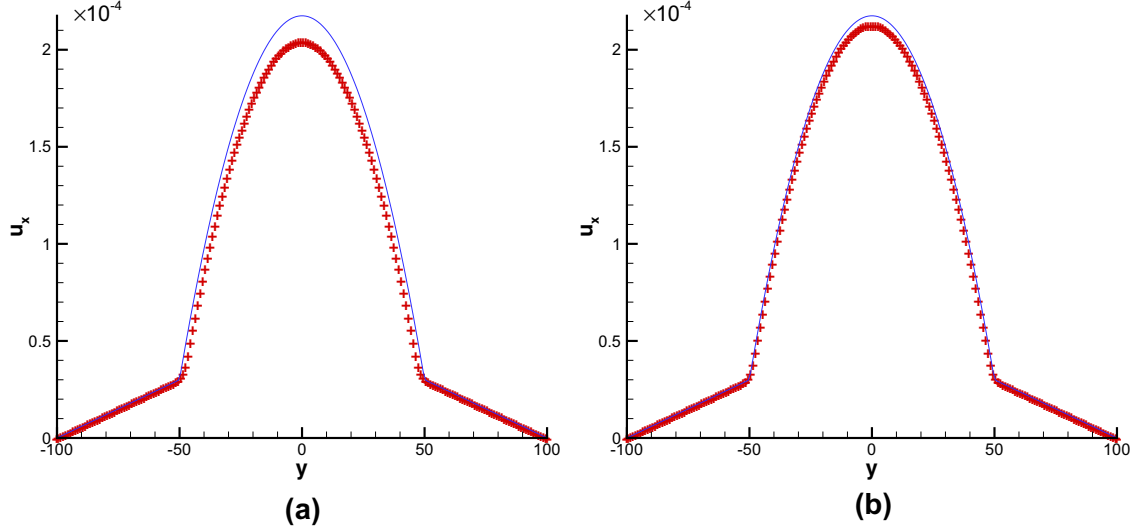


Fig. 4. Comparison of the velocity profiles obtained by using the present LB model with τ defined by Eq. (19) in (a) and by Eq. (20) in (b) with the analytical solutions for $G_R = 1.5 \times 10^{-8}$, $G_B = 0$ and $M = 0.08$. The discrete symbols represent the numerical results and the solid lines are the analytical solutions from Eq. (25).



Fig. 5. Simulation setup for capillary intrusion. The intruding (blue) fluid is the wetting phase while the defending (red) fluid is the non-wetting phase. The portion in the center of the domain is a capillary tube of length L . (For interpretation of the references to color in this figure legend, the reader is referred to the web version of this article.)

be seen that our color-fluid model can predict Eq. (28) reasonably well for both viscosity ratios.

3.2. Numerical investigation of LCO_2 displacing water in a 2D dual-permeability pore network: comparison with micromodel experiments

Although a number of micromodel experiments have been performed focusing on fundamental processes at the pore scale during CO_2 injection into a porous formation, they are all limited to qualitative visualizations of the displacement mechanisms except a recent experimental study by Zhang et al. [9], which quantitatively evaluated the impacts of porous media heterogeneity and capillary number on CO_2 -water displacement. Note that the capillary number describes the relative magnitude of viscous to capillary forces and is defined as $Ca = \frac{u_n \eta_n}{\sigma \cos(\theta)}$, where u_n and η_n are the average velocity and dynamic viscosity of the advancing non-wetting fluid,

respectively. The interesting outcomes and detailed experimental data in [9] motivate us to numerically investigate LCO_2 displacement of water in a 2D microfluidic porous media geometry (see Fig. 7), which consists of one inlet section and one outlet section, connected by a pore network. The pore network contains two distinct permeability zones with each occupying approximately one-half-width of the domain. The high (low) permeability zone consists of a staggered periodic array of uniform circular grains, 108(54) μm in diameter, with 84(42) μm pore bodies, 27.7(13.9) μm pore throats, and a porosity of 0.5. Table 1 gives the geometrical parameters and fluid properties used in our LB simulations along with those used in micromodel experiments of Zhang et al. [9]. In the simulations, we choose pore throat widths similar to the experiments so that the magnitudes of capillary pressure are maintained at the same level. However, in comparison with the experiments, we have neglected the effect of depth and

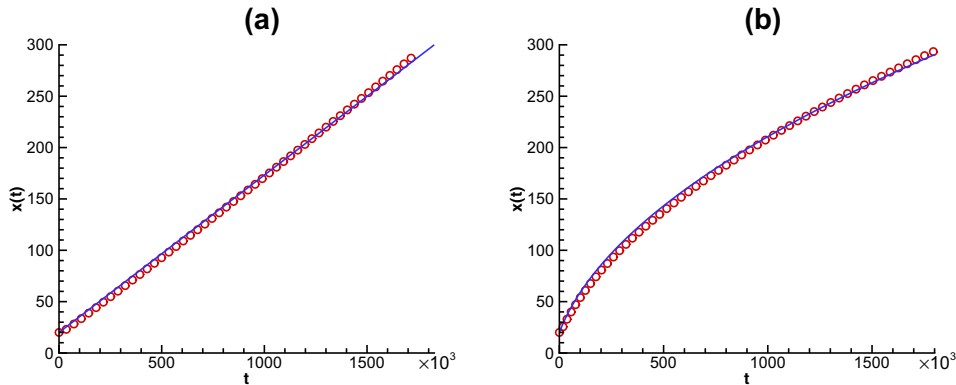


Fig. 6. The length of the column of the intruding fluid, $x(t)$, as a function of time for the viscosity ratios of (a) $M = 1$ and (b) $M = 0.1$. The open circles represent simulation results and the solid lines are the theoretical predictions from Eq. (28).

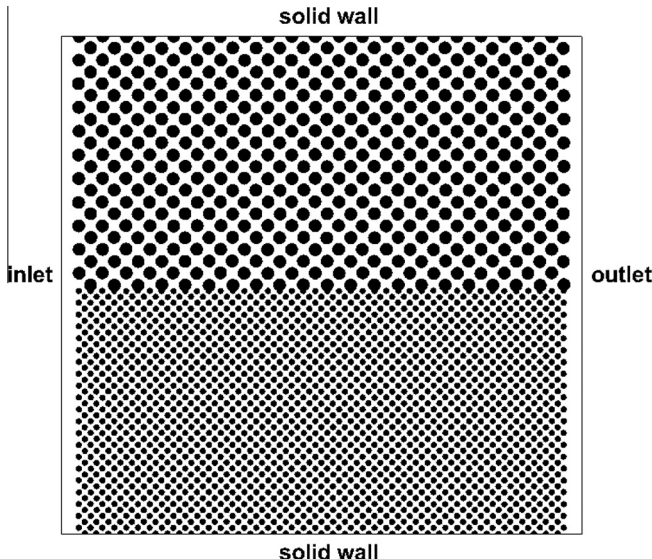


Fig. 7. Schematic diagram of the dual-permeability microfluidic system in the simulations and the setup of the boundary conditions. The black circles represent the solid grains.

Table 1

Comparison of geometrical and fluid properties used in the present simulations and previous micromodel experiments [9].

	Simulations	Experiments
Length [cm]	0.408	1.22
Width [cm]	0.403	1.21
Depth [μm]	–	35
Porosity (H/L) ^a	0.5/0.5	0.3987/0.3987
Grain diameter (H/L) [μm]	108/54	200/100
Pore body length (H/L) [μm]	84/42	120/60
Pore throat length (H/L) [μm]	27.7/13.9	26.7/13.3
Density ratio ($\text{LCO}_2/\text{water}$)	1.0	0.827
Viscosity ratio ($\text{LCO}_2/\text{water}$)	0.08	0.08
Contact angle [deg]	15.0	15.3 ± 1.9

^a H : high permeability zone, L : low permeability zone.

simulated the pore network with smaller domain size and higher porosity in order to minimize computing cost. Currently, it is challenging to simulate the exact experimental 2D pore network with the present grid accuracy (i.e., $\delta_x = 1.5 \mu\text{m}$) because the number of lattice grids will be roughly 9 times that used in the present system (2816×2689), which is far beyond our computing capacity. In addition, simulation of the experimental system will take much longer to reach quasi-steady state (i.e., when the variation in saturation of LCO_2 (S_{LCO_2}) meets the criterion:

$$\left| \frac{S_{\text{LCO}_2}(t) - S_{\text{LCO}_2}(t-10^4)}{S_{\text{LCO}_2}(t)} \right| \leq 10^{-4}$$

due to its larger size compared to the present computational domain. The density difference between LCO_2 and water is not taken into account since the experiments are conducted in a horizontally placed micromodel with a small depth, where the gravity effect is largely suppressed.

Initially, the pore network is fully saturated with the wetting fluid (water). The non-wetting LCO_2 is injected continuously with a constant flow rate at the left inlet, while a constant pressure is imposed at the right outlet. The lateral boundaries are assumed to be solid walls. In the simulations, a total of seven different inlet flow rates are used, leading to capillary numbers ranging from $\log Ca = -4.36$ to $\log Ca = -3.06$. The two-phase displacement process is expected to be unstable because of the unfavorable viscosity ratio ($\log M = -1.1$) between the invading LCO_2 and the defending water. We run the simulation until a steady state LCO_2 saturation is obtained for each of the capillary numbers.

Fig. 8 shows the final fluid distributions in the dual-permeability system at several selected capillary numbers when the non-wetting LCO_2 is injected. Fingering is clearly observed during the LCO_2 displacement, which is attributed to the non-homogeneous permeability at the microscopic pore scale. Three representative flow patterns are identified depending on the magnitude of the capillary number. At low capillary numbers, i.e., $\log Ca = -4.36$ and -4.16 , the LCO_2 displaces water only in the high permeability zone because the higher entry pressure prevents the non-wetting fluid from entering the low permeability zone. As the capillary number increases, the pressure drop increases across the more viscous wetting fluid. The entry pressure of the low permeability zone is overcome when $\log Ca = -4.06$, and thus the non-wetting fluid can enter this zone. However, the non-wetting fluid cannot completely break through the low permeability zone at $\log Ca = -4.06$, implying that the pressure drop is not large enough to form a continuous flow across this zone even though it is able to overcome the entry pressure. Note that the critical capillary number (Ca_c), above which displacement occurs across the low permeability zone, is in the range of $-4.16 < \log Ca_c < -4.06$ in our simulations, which is slightly smaller than the experimental finding ($-3.96 < Ca_c < -3.66$) of Zhang et al. [9]. This is likely caused by the lower flow resistance due to larger porosity of the pore network used in our simulations, allowing the non-wetting fluid to more readily intrude the pore bodies. At high capillary numbers ($\log Ca \geq -3.59$), we can observe complete LCO_2 breakthrough in both zones since the displacement pressure is increased enough to maintain continuous flows through these zones.

The simulation results presented in **Fig. 8** also exhibit displacement characteristics associated with capillary and viscous fingerings, which occur at different capillary numbers in the high and low permeability zones. First, we describe the characteristics of fingering patterns in the high permeability zone. At low capillary numbers (e.g., $\log Ca = -4.36$), the pore body is almost occupied completely by the advancing LCO_2 before the LCO_2 can reach a neighboring pore, consistent with previous numerical observations in a homogeneous pore network [23]. The LCO_2 flow traverses the main flow direction and fingers sometimes progress into new pore bodies in the backward direction, indicating capillary fingering [64,95]. In capillary fingering, capillarity is the principal force and, hence, the displacing fluid progresses preferentially from a pore through the largest pore throat in any direction. In addition, we also notice that the trapped blobs of water occupy considerably more than four pore bodies at small capillary numbers; whereas they decrease in size with an increase in capillary number. At higher capillary numbers (typically $\log Ca \geq -3.59$), a finger often only occupies partial pore bodies it passes through (see, e.g., inside the white box in **Fig. 8(d)**). Multiple loosely connected or disconnected fingers mainly progress forward toward the outlet boundary with limited or no lateral flows, and are referred to as viscous fingers [64,95]. In viscous fingering, the capillary force and pressure drop over the displacing fluid is negligible, and the dominant force is due to the viscosity of the wetting fluid. The dominant viscous force causes some fingers to break up, leading to some isolated blobs of LCO_2 distributed in the pores (see **Fig. 8(d)–(f)**, in particular, e.g. inside the white box in **Fig. 8(e)**). In the low permeability zone, lateral LCO_2 displacement is clearly seen for all the cases of $Ca > Ca_c$, which again shows the typical characteristics of capillary fingering. This result suggests that the flow rate through the low permeability zone is lower than the high permeability zone for each case. As observed in the high permeability zone, the trapped blobs of water in the low permeability zone also decrease in size with the increase of the capillary number. We interestingly note that the LCO_2 flow in the low permeability zone mainly originates from the inlet section but that LCO_2 fingers from the high permeability zone can also be found at a

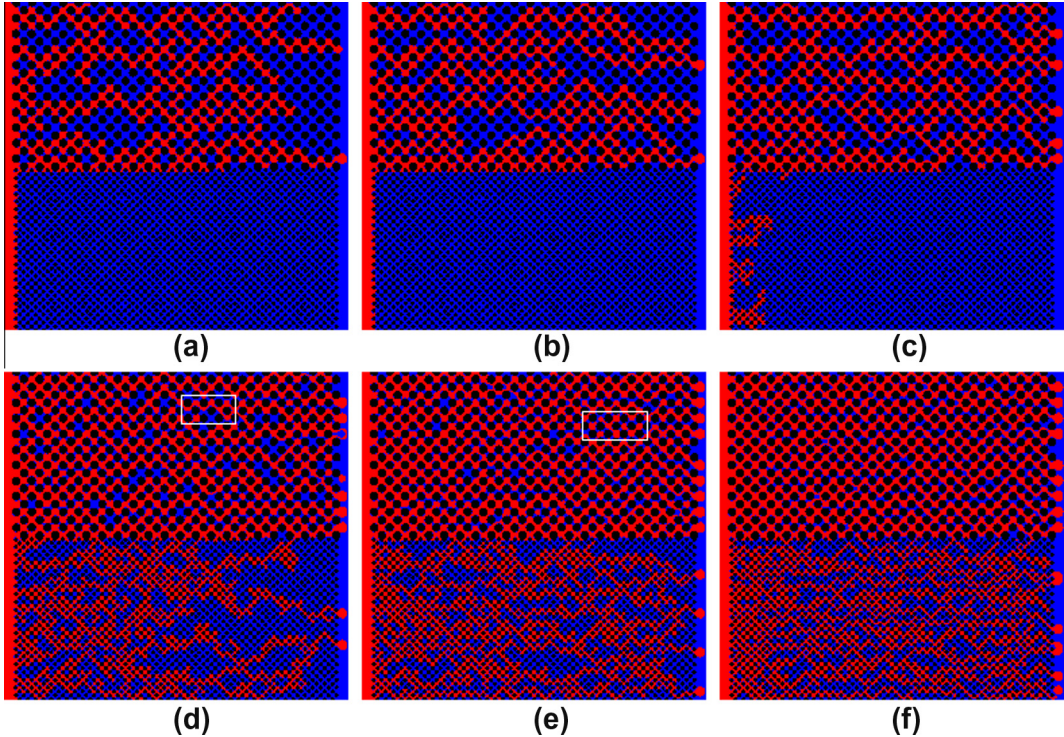


Fig. 8. Final fluid distributions in the dual-permeability microfluidic system at various capillary numbers: (a) $\log Ca = -4.36$, (b) $\log Ca = -4.16$, (c) $\log Ca = -4.06$, (d) $\log Ca = -3.59$, (e) $\log Ca = -3.36$, (f) $\log Ca = -3.06$. LCO₂ and water are shown in red and blue, respectively. The white rectangular boxes are used to guide the reader's eyes. (For interpretation of the references to color in this figure legend, the reader is referred to the web version of this article.)

few isolated locations, in agreement with Zhang et al. [9]. As the capillary number increases, the number of LCO₂ flow paths connected to the outlet section increases from 2 to 16 in the entire pore network. The increase in the number of flow paths does not necessarily imply that the volume fraction of LCO₂ residing in active flow paths increases with the capillary number because the lateral flow also contributes to the volume of LCO₂ in each active flow path. This may explain why Zhang et al. [9] observed that the volume fraction of LCO₂ in active flow paths sometimes decreased with an increase in Ca .

To illustrate how the fingers develop in both permeability zones, Fig. 9 shows the drainage process of LCO₂ in the dual-permeability system at $\log Ca = -4.06$, where the incomplete breakthrough occurs in the low permeability zone. The dimensionless time is defined by $t^* = u_n t / H$, where H is the width of computational domain. At the early stages, the LCO₂ fingers only invade the high permeability zone. As the fingers in the high permeability zone lengthen, the pressure loss increases resulting in some LCO₂ preferentially flowing into the low permeability zone. However, the invading speed in the high permeability zone is much faster than that in the low permeability zone. In Fig. 9(c), it can be observed in the high permeability zone that one of the LCO₂ fingers passes through the outlet boundary, but such a single flow path cannot accommodate all the incoming LCO₂ from the inlet. Therefore, the other fingers still keep progressing in both high and low permeability zones. At $t^* = 0.242$, five LCO₂ flow paths are connected to the outlet boundary in the high permeability zone. This number subsequently remains unchanged while some local flows still change slowly in the high permeability zone until the system reaches steady state.

To illustrate the displacement efficiency, we plot the pore volume fraction S_{LCO_2} of LCO₂ at steady state (i.e., the LCO₂ saturation) as a function of $\log Ca$ in Fig. 10. The LCO₂ saturation in the entire pore network increases with an increase in Ca . Specifically, the increase is relatively insignificant at the two lowest capillary

numbers and at the three highest capillary numbers, whereas a significant increase is observed in the range of $-4.06 \leq \log Ca \leq -3.36$, especially when the displacement in the low permeability zone converted from incomplete to complete breakthrough. The LCO₂ saturation in the high permeability zone increases linearly with $\log Ca$ until $\log Ca = -3.36$, above which the saturation remains nearly constant. The approximate linear relationship between the displacing fluid saturation and $\log Ca$ was also observed by Zhang et al. [64] in drainage experiments conducted in a homogeneous water-wet pore network micromodel with precisely microfabricated pore structures. At the four highest capillary numbers, with complete breakthrough occurring in both permeability zones, the LCO₂ saturation in the high permeability zone is much higher than that in the low permeability zone, which is caused by the different displacement mechanisms that are dominant in these zones, i.e., viscous fingering in the high permeability zone and capillary fingering in the low permeability zone. Fig. 10 also gives the pore-scale experimental data of Zhang et al. [9], which are plotted by the solid symbols, for comparison. The figure shows that our numerical results are qualitatively consistent with their experimental measurements. The quantitative differences could be mainly attributed to the differences in pore networks—such as grain size, porosity, and permeability.

Besides the fluid saturations, the interfacial areas between LCO₂ and water are also calculated. In CO₂ sequestration, the CO₂-brine interfacial areas play a vital role in the mass transfer kinetics, such as CO₂ dissolution in the formation brine and subsequent geochemical reactions with brine and host rock [5]. Following the work of Zhang et al. [9], we use the interfacial length instead of the interfacial area in the present 2D simulations. This length includes the length of LCO₂-water interfaces in the pore bodies and throats and the length of the wetting films between the LCO₂ and the grain surfaces. Fig. 11(a) plots the specific interfacial length (l_s) as a function of S_{LCO_2} in the entire pore network, where the specific interfacial length is defined as the ratio of the interfacial length to the pore

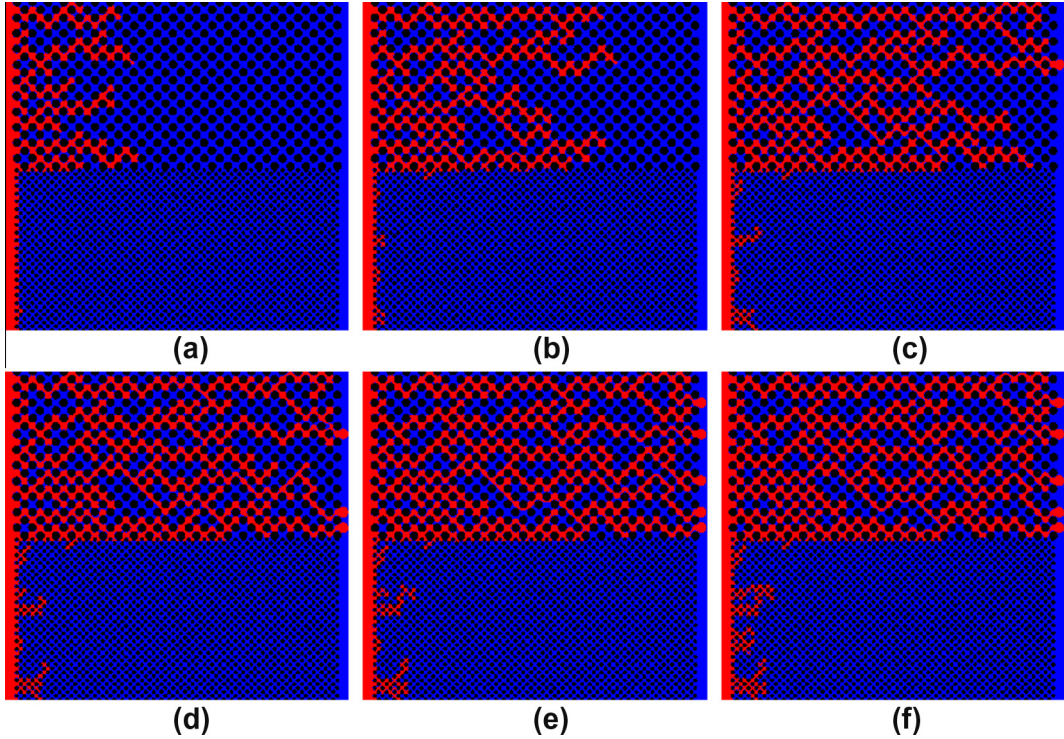


Fig. 9. LCO₂ distribution in the dual-permeability microfluidic system for log Ca = -4.06 at (a) $t^* = 0.048$, (b) $t^* = 0.097$, (c) $t^* = 0.145$, (d) $t^* = 0.193$, (e) $t^* = 0.242$, (f) $t^* = 0.403$. LCO₂ and water are shown in red and blue, respectively. (For interpretation of the references to color in this figure legend, the reader is referred to the web version of this article.)

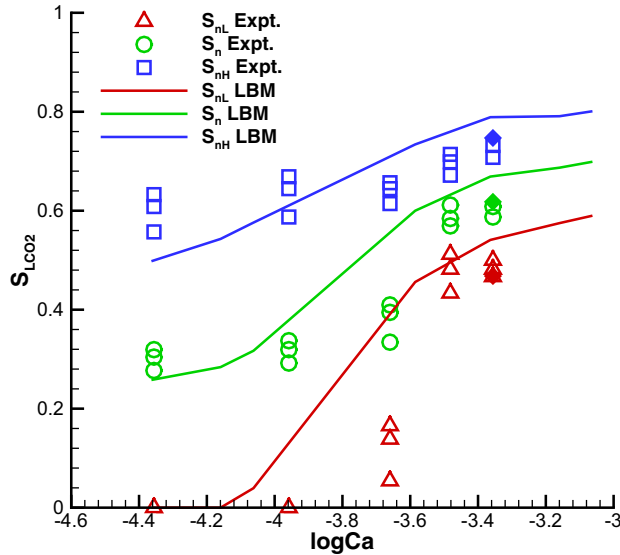


Fig. 10. LCO₂ saturation as a function of the capillary number (expressed as log Ca) in the low (S_{nl}) and high permeability zones (S_{nh}), and over the entire pore network (S_n). The solid lines represent the simulation results, and the discrete hollow symbols are the experimental data of Zhang et al. [9]. Note that the discrete solid diamond symbols represent the simulation results in a dual-permeability pore network with experiment-matched porosity and grain size but a smaller domain size.

area. We find that the simulation data can be correlated by a power-law relationship between l_s and S_{LCO_2} , i.e.,

$$l_s = k S_{LCO_2}^\alpha \quad (29)$$

where k and α are the fitting parameters, which primarily depend on the geometry of porous media. Based on least-square fitting,

the resulting equation is $l_s = 827.75 S_{LCO_2}^{1.35}$. At low and high injection rates, which are bounded based on whether the LCO₂ completely breaks through the low permeability zone, the specific interfacial length is a linearly increasing function with S_{LCO_2} . The slope at high injection rates is larger than at low injection rates, consistent with the previous experimental observations [9]. It is worth noting that the experimental data in Ref. [9] also correlate well with Eq. (29) for the fitting parameters $k = 523.19$ and $\alpha = 1.36$ over the whole range of flow conditions considered (see Fig. 11(b)). In addition, it can be found that the maximum specific interfacial length in our simulations is much larger than in the experiments, which is attributed to two reasons: first, a higher saturation is achieved due to the larger Ca used in our simulations; second, the maximum specific interfacial length is 700 cm⁻¹ in our simulations, significantly larger than the extreme value of 460 cm⁻¹ in the experiments. A discussion of this topic will be shown in the next section.

Although the physics involved in immiscible two-phase displacement is correctly captured in our simulations, the quantitative difference is still significant between the simulations and experiments. One possible reason for this difference can be attributed to the mismatch between the simulation and experimental systems. Therefore, it is anticipated that the difference will decrease if the simulated pore network matches more closely the experimental one. Fig. 12 shows the final fluid distribution for log Ca = -3.36 and M = 0.08 in a dual-permeability system, which includes a pore network exactly matching the experiment of Zhang et al. [9] except a smaller physical domain is considered. Note that the maximum value of specific interfacial length is 462 cm⁻¹ in this pore network, very close to the one (460 cm⁻¹) in the experiments. Consistent with the experimental observation, breakthrough of the non-wetting fluid occurs in both low and high permeability zones. Also, the displacement reveals primarily viscous fingering in the high permeability zone and capillary fingering in the low permeability zone. We also calculate the saturation of

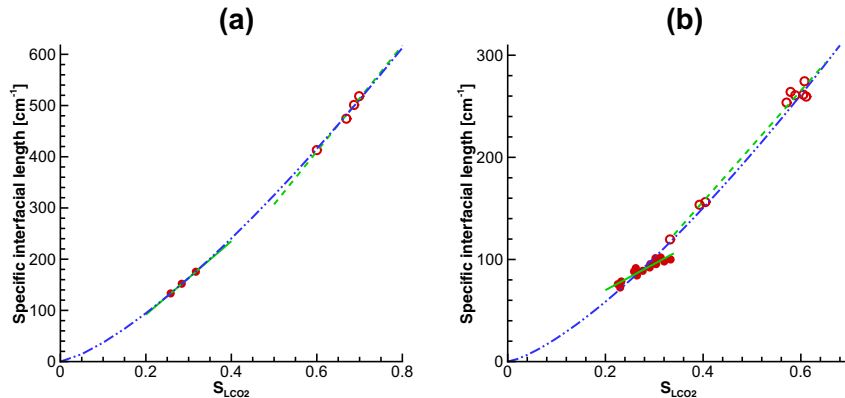


Fig. 11. LCO₂–water specific interfacial length (cm⁻¹) as a function of the LCO₂ saturation in the dual-permeability pore network for (a) the LB simulations and (b) the experiments of Zhang et al. [9]. The data at low (represented by red solid symbols) and high injection rates (represented by red open symbols) both exhibit a linear relationship between the specific interfacial length and the LCO₂ saturation, as indicated by the green solid line and the green dashed line, respectively. The dash-dot-dot lines are the fitting results of Eq. (29), where $k = 827.75$ and $\alpha = 1.35$ with the coefficient of determination $R^2 = 0.999$ for (a), and $k = 523.19$ and $\alpha = 1.36$ with the coefficient of determination $R^2 = 0.982$ for (b). (For interpretation of the references to color in this figure legend, the reader is referred to the web version of this article.)

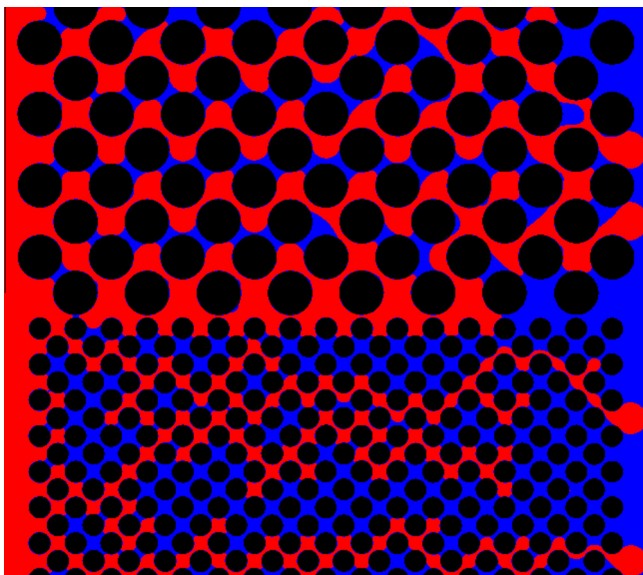


Fig. 12. Final fluid distribution for $\log Ca = -3.36$ and $M = 0.08$ in a dual-permeability system that includes a pore network exactly matched the experiment of Zhang et al. [9] except a smaller physical domain is considered. LCO₂ and water are shown in red and blue, respectively. (For interpretation of the references to color in this figure legend, the reader is referred to the web version of this article.)

non-wetting fluid in each permeability zone and in the entire pore network, which are represented by solid diamond symbols in Fig. 10 for comparison. As anticipated, the present simulation results exhibit better agreement with the experimental data of Zhang et al. [9] than those obtained in the previous pore network with porosity of 0.5.

3.3. Numerical investigation of LCO₂ displacing water in a 2D heterogeneous pore network in comparison with dual-permeability case

Having verified that our LB simulations can reproduce the overall fingering patterns observed in the experiments, we investigate LCO₂ displacement of water in a heterogeneous pore network (see Fig. 14), which is generated by assuming a uniform distribution of grain diameters ranging from 42 μm to 132 μm, and a

uniform distribution of grain locations. Any two circular grains are not allowed to overlap and the gap between any two grains is not less than 5 grids. The pore network has the same size and porosity as the dual-permeability pore network described in Table 1, which allows for a direct comparison between the two-phase displacements. In addition, we keep the same fluid pair and specify the same initial and boundary conditions as described in last section.

Due to the limitation of computing resources, we examine the dependence of numerical results on the grid size in a smaller physical domain, which is constructed by taking a slice of 0.144×0.144 cm² from the left lower side of the heterogeneous pore network. The capillary number is chosen as $\log Ca = -3.7$. Fig. 13(a) shows the final fluid distribution in the coarse grid with the minimum grain gap of 5 grids and (b) shows the final fluid distribution in the fine grid with the minimum grain gap of 10 grids. It is clearly seen that the grid refinement only has a slight effect on the numerical results (the LCO₂ saturation and the specific interfacial length vary from 0.424 and 182.5 cm⁻¹ in the coarse grid to 0.414 and 178.3 cm⁻¹ in the fine grid, a difference of 2.42% and 2.36%, respectively), indicating that the coarse grid with the minimum grain gap of 5 grids can provide acceptable numerical accuracy.

Fig. 14 shows the final fluid distributions in the heterogeneous microfluidic system at various Ca with LCO₂ injected from the left inlet to displace water. As Ca increases, we can clearly observe the transition from capillary to viscous fingering, occurring at around $\log Ca = -4.06$. A strong indication of viscous fingering is that some LCO₂ fingers are stretched very thin and even break up due to the dominant viscous force from the more viscous wetting fluid. Note that in the dual-permeability pore network this feature of viscous fingering is observed at a lower capillary number of $\log Ca = -4.16$, because the lateral flow patterns are largely confined in high permeability zone, resulting in a smaller flow resistance and a higher local flow velocity. As Ca increases, the size of the trapped water blobs decreases but the number of LCO₂ flow paths connected to the outlet boundary increases, which is consistent with the observations in the dual-permeability pore network.

Fig. 15 shows the simulated LCO₂ saturation as a function of $\log Ca$ for the heterogeneous and the dual-permeability pore network. The LCO₂ saturation roughly increases linearly with $\log Ca$ in the heterogeneous pore network, whereas in the dual-permeability pore network a considerable increase is observed when the capillary number increases from $\log Ca = -4.06$ to -3.59 . It

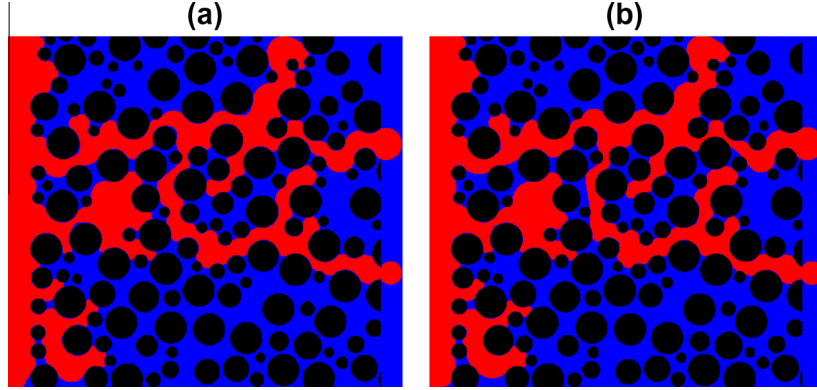


Fig. 13. Final fluid distribution in (a) the coarse grid and (b) the fine grid for $\log Ca = -3.7$ and $M = 0.08$. In the coarse grid, the minimum grain gap is 5 grids with each grid corresponding to $1.5 \mu\text{m}$; whereas in the fine grid, the minimum grain gap is 10 grids with each grid corresponding to $0.75 \mu\text{m}$. Note that LCO_2 and water are shown in red and blue, respectively. (For interpretation of the references to color in this figure legend, the reader is referred to the web version of this article.)

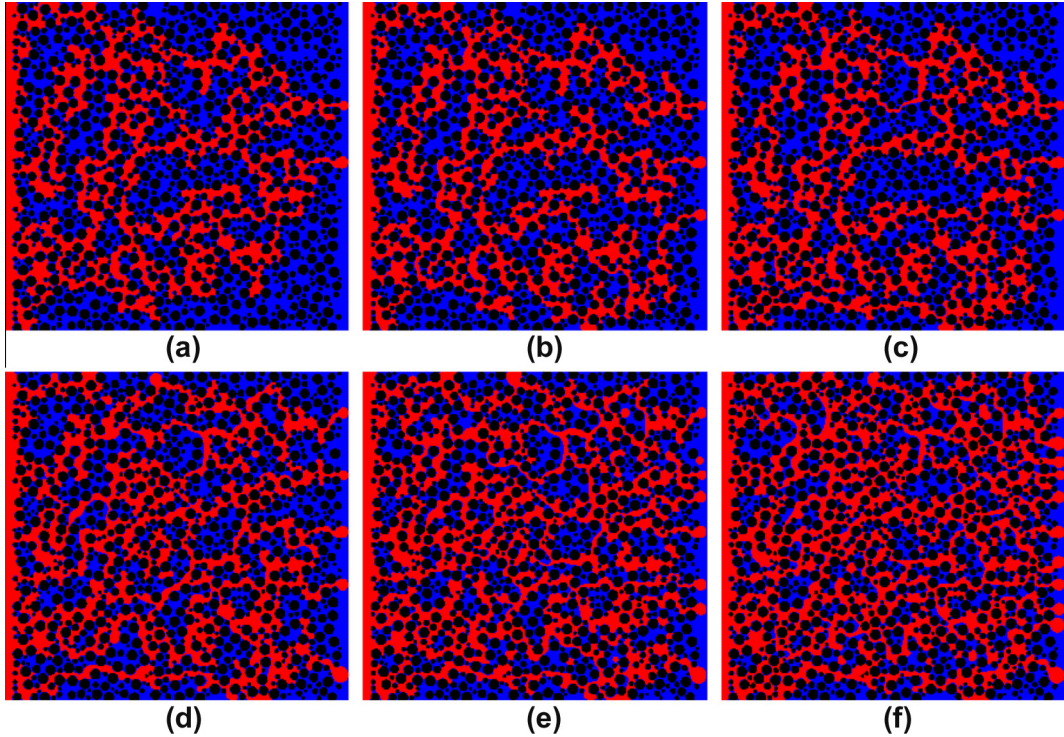


Fig. 14. Final fluid distributions in the randomly heterogeneous system at (a) $\log Ca = -4.36$, (b) $\log Ca = -4.16$, (c) $\log Ca = -4.06$, (d) $\log Ca = -3.59$, (e) $\log Ca = -3.36$, (f) $\log Ca = -3.06$. LCO_2 and water are shown in red and blue, respectively. (For interpretation of the references to color in this figure legend, the reader is referred to the web version of this article.)

should be noted that drainage experiments in a homogeneous micromodel [64] indicate that unstable displacement through capillary and viscous fingering also leads to an approximately linear increase in non-wetting fluid saturation with $\log Ca$. Compared with the dual-permeability pore network, the LCO_2 saturation is higher at low capillary numbers but is lower at high capillary numbers. The difference occurs because, at low capillary numbers, the preferential flow paths can be formed more easily due to heterogeneity in the pore throat size, while the LCO_2 flow paths are restricted in the high permeability zone in the dual-permeability pore network; at high capillary numbers, smaller throats (e.g. the throat has a smallest width of $7.5 \mu\text{m}$ in contrast to $13.9 \mu\text{m}$ in the dual-permeability pore network) are randomly distributed in the heterogeneous pore network, which make it harder for the LCO_2 to enter their neighboring pore bodies. It is expected that

the LCO_2 saturation in the heterogeneous pore network will get closer to that in the dual-permeability pore network as more small pores are intruded when Ca continues to increase.

Fig. 16 plots the specific interfacial length as a function of the LCO_2 saturation. As observed in the dual-permeability pore network, the specific interfacial length monotonously increases with the LCO_2 saturation. The specific interfacial length also exhibits a power-law dependence on the LCO_2 saturation, i.e., $l_s = 550.89S_{\text{LCO}_2}^{1.42}$. Obviously, the fitting parameters k and α are different in both pore networks that we investigate, again suggesting that they are geometry-dependent. Previous pore-scale displacement experiments in a homogeneous micromodel [64] have shown that the specific interfacial length is linearly proportional to S_{LCO_2} , which corresponds to a special case of Eq. (29), i.e., with $\alpha = 1$. We also used the present LB model to conduct the drainage

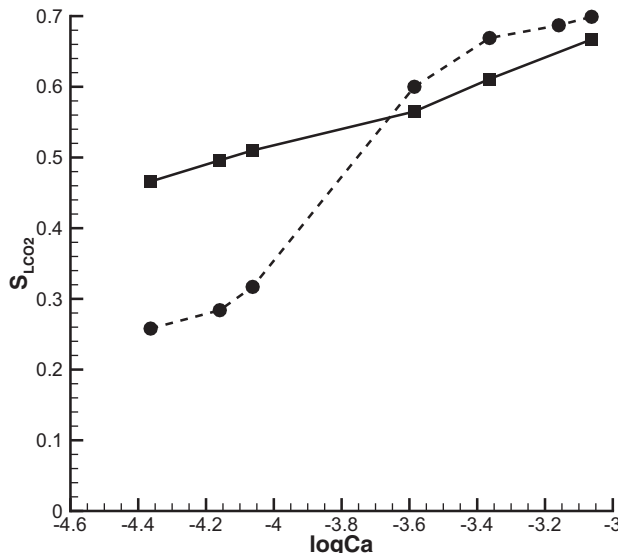


Fig. 15. LCO₂ saturation as a function of the capillary number (expressed as log Ca) in the randomly heterogeneous (represented by squares and solid line) and dual-permeability pore networks (represented by circles and dashed line).

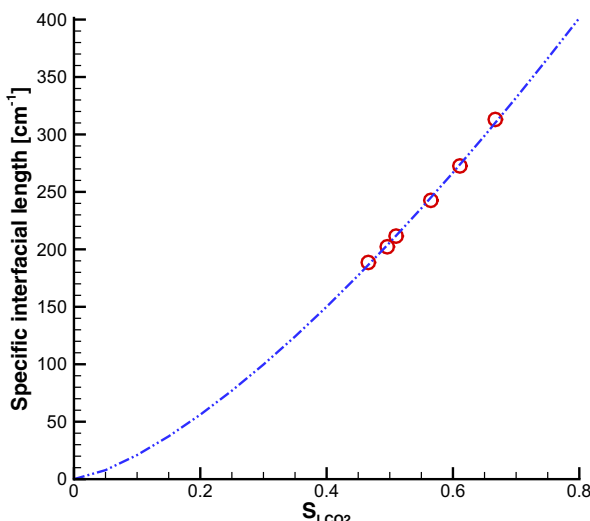


Fig. 16. LCO₂-water specific interfacial length (cm⁻¹) as a function of the LCO₂ saturation in the randomly heterogeneous pore network. The open symbols represent the simulation results, and the dash-dot-dot line is the fitting results of Eq. (29), where $k = 550.89$ and $\alpha = 1.42$ with the coefficient of determination $R^2 = 0.998$.

simulations in a homogeneous pore network consisting of a staggered periodic array of uniform circular grains, similar to the one used by Zhang et al. [64], and found that the linearly proportional relationship was reproduced (not shown here). In this sense, the exponent α in Eq. (29) is primarily determined by the geometrical configuration, particularly, $\alpha \approx 1$ for homogeneous pore networks, and $\alpha \approx 1.35$ for dual-permeability pore networks. Finally, we conclude that Eq. (29) provides a generalized expression that correlates the specific interfacial length with the saturation of non-wetting fluid in various porous media geometries.

3.4. Comparison of numerical results obtained by BGK approximation and MRT scheme

It is well-known that in single-phase flows the exact location of solid boundary in the BGK LB model depends on the fluid viscosity [65,96,97]. The viscosity-dependent boundary conditions pose a severe problem for simulating flow through porous media because the absolute permeability becomes viscosity dependent. To overcome this problem, a possible solution is to replace the BGK approximation with a MRT scheme [68,97–99]. The capability of the MRT schemes was extensively tested on synthetic model structures such as fiber materials [96,100], body-centered cubic arrays of spheres and random-sized sphere packings [97,100], and on real micro-/nanostructures obtained through X-ray computed tomograph [101–103]. It has been analytically and numerically demonstrated that the most efficient MRT scheme, namely two-relaxation-time (TRT), can yield viscosity-independent results with the bounce-back boundary condition applied at solid walls [97,98]. Due to the inherent ‘deficiency’ of BGK model, it is imperative to confirm that the simulation results presented in Sections 3.1–3.3 are viscosity-independent. To investigate this question, we simulate LCO₂ displacement of water in a homogeneous pore network by the use of color-fluid model with both the BGK approximation and TRT scheme. The pore network consists of a staggered periodic array of uniform circular grains, 60 μm in diameter, with 70 μm pore bodies, 13.9 μm pore throats, and a porosity of 0.37. The width of pore throats is equal to that in the previous dual-permeability pore network, leading to the same number of lattice grids distributed in each pore throat for both pore networks. The whole computational domain has a size of 876 × 768 μm², and the capillary number and the viscosity ratio are chosen as log Ca = -3.52 and $M = 0.08$, respectively.

Fig. 17(a) and (b) show the final fluid distributions obtained by the BGK model and the TRT model, respectively. The relaxation time is $\{\tau_R, \tau_B\} = \{0.59, 1.625\}$. Note that the free relaxation parameters s_1, s_2 and s_4 are chosen as $s_1 = s_2 = \frac{1}{\tau}$ and $s_4 = \frac{8(2-s_1)}{8-s_1}$

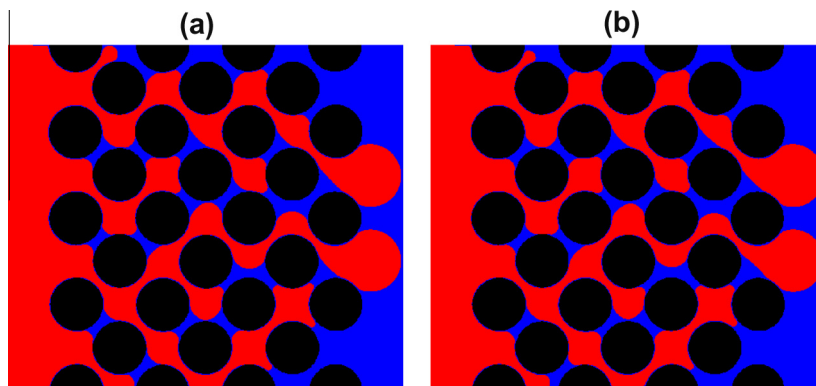


Fig. 17. Final fluid distributions obtained by (a) the BGK model and (b) the TRT model. The capillary number and the relaxation time are chosen as log Ca = -3.52 and $\{\tau_R, \tau_B\} = \{0.59, 1.625\}$. LCO₂ and water are shown in red and blue, respectively. (For interpretation of the references to color in this figure legend, the reader is referred to the web version of this article.)

in the TRT model. It can be seen that the both models produce almost the same results. We also calculate the LCO₂ saturation and the specific interfacial length and find that their values are 0.71 and 457 cm⁻¹ for the BGK model and 0.694 and 450 cm⁻¹ for the TRT model. The similarity in simulation results suggests that the BGK model is able to simulate porous media flows with reasonable accuracy, in apparent contradiction to the previously reported numerical findings [97,100]. Actually, the viscosity-dependent numerical results in the BGK model are mainly attributed to insufficient grid resolution [99], which can lead to high Knudsen number where the flow is at the onset of the slip regime [104]. Once the pore space is sufficiently resolved such that grid-independent numerical results are obtained, the BGK model will also yield reasonably accurate results as the MRT model does. To further verify this, we conduct a simulation with another pair of viscosity/relaxation time, i.e., {τ_R, τ_B} = {0.545, 1.0625} for the homogeneous pore network shown in Fig. 17 at the same Ca and M. It is found that the LCO₂ saturation and the specific interfacial length are 0.691 and 447 cm⁻¹ for {τ_R, τ_B} = {0.545, 1.0625} and 0.71 and 457 cm⁻¹ for {τ_R, τ_B} = {0.59, 1.625}. The small variation in numerical results indicates that the BGK model is able to produce results similar to MRT/TRT for these two selected pairs of relaxation time. We therefore conclude that the simulation results presented in Sections 3.1–3.3 are viscosity-independent even though only the BGK model is used. But it is worth emphasizing that the MRT model has great potential in the simulation of porous media flows because it can ensure viscosity-independent solutions on a relatively coarse grid.

4. Conclusions

In this paper, we extend our previously developed lattice Boltzmann color-fluid model [58] to simulate two-phase flows in complex porous media. We introduce an expression for viscosity of a fluid mixture to account for different kinematic viscosities of both fluids, and model the fluid-surface interactions by assigning the value of the phase field at the solid walls. The capability and accuracy of the model is first validated by simulating immiscible layered two-phase flow between two infinite plates and dynamic capillary intrusion. The model is then used to simulate the LCO₂ displacement of water in a dual-permeability pore network. The extent and behavior of LCO₂ preferential flow (i.e., fingering) is found to depend on Ca. Three different displacement patterns observed in the experiments of Zhang et al. [9] are reproduced: (1) LCO₂ displaces water only in the high permeability zone at low Ca; (2) as Ca increases, the LCO₂ enters the low permeability zone but cannot completely break through; (3) at high Ca, complete CO₂ breakthrough occurs in the low permeability zone. The predicted variation of LCO₂ saturation with Ca, as well as variation of the specific interfacial length with LCO₂ saturation, are both in qualitative agreement with the experimental observations, and the quantitative differences are mainly attributed to the differences in the pore networks. We also simulate liquid LCO₂ displacement of water in a randomly heterogeneous pore network, which has the same size and porosity as the dual-permeability network. It is observed that the transition from capillary to viscous fingering occurs at log Ca = -4.06, which is slightly higher than for the dual-permeability pore network. In comparison with the dual-permeability case, the LCO₂ saturation is higher at low Ca but is lower at high Ca, and we have not observed significant increase in the LCO₂ saturation over the whole range of Ca we consider. The simulation results in either pore network show that the specific interfacial length and the LCO₂ saturation can be well correlated by a power-law relationship, which also works well for the experimental data of Zhang et al. [9].

Acknowledgments

The authors gratefully acknowledge the support from the LDRD Program (20100025DR and 20140002DR) of Los Alamos National Laboratory and from the International Institute for Carbon Neutral Energy Research (WPI-I2CNER), sponsored by the Japanese Ministry of Education, Culture, Sports, Science and Technology. Dr. Mart Oostrom's contribution has been supported by the "Pore-Scale Modeling" Research Campaign at EMSL, a national scientific user facility sponsored by the Department of Energy's Office of Biological and Environmental Research and located at Pacific Northwest National Laboratory, operated by Battelle for the US Department of Energy under Contract DE-AC05-76RL01830. We also acknowledge the computing support from LANL Institutional Computing Program. We thank Dr. Changyong Zhang, currently at Exxon-Mobil, for his assistance with analyzing and interpreting the results of the dual-permeability micromodel experiments he performed while at PNNL.

References

- [1] Bachu S, Adams J. Sequestration of CO₂ in geological media in response to climate change: capacity of deep saline aquifers to sequester CO₂ in solution. *Energy Convers Manage* 2003;44(20):3151–75. [http://dx.doi.org/10.1016/S0196-8904\(03\)00101-8](http://dx.doi.org/10.1016/S0196-8904(03)00101-8).
- [2] Pacala S, Socolow R. Stabilization wedges: solving the climate problem for the next 50 years with current technologies. *Science* 2004;305(5686):968–72. <http://dx.doi.org/10.1126/science.1100103>.
- [3] Oloruntobi, T. LaForce, Effect of aquifer heterogeneity on CO₂ sequestration, in: Proceedings of the SPE EUROPEC/EAGE Annual Conference and Exhibition, Society of Petroleum Engineers, Amsterdam, The Netherlands, 2009, p. SPE 121776. <http://dx.doi.org/10.2118/121776-MS>.
- [4] Riazi M, Sohrabi M, Bernstein C, Jamilahmady M, Ireland S. Visualisation of mechanisms involved in CO₂ injection and storage in hydrocarbon reservoirs and water-bearing aquifers. *Chem Eng Res Des* 2011;89(9):1827–40. <http://dx.doi.org/10.1016/j.cherd.2011.03.009>.
- [5] Iglesias S. Dissolution trapping of carbon dioxide in reservoir formation brine—a carbon storage mechanism. InTech; 2011. <http://dx.doi.org/10.5772/20206> [chapter 10].
- [6] Cinar Y, Riaz A, Tchelepi H. Experimental study of CO₂ injection into saline formations. *SPE J SPE* 2009;110628:588–94. <http://dx.doi.org/10.2118/110628-PA>.
- [7] Chalbaud C, Robin M, Lombard J-M, Martin F, Eggermann P, Bertin H. Interfacial tension measurements and wettability evaluation for geological CO₂ storage. *Adv Water Resour* 2009;32(1):98–109. <http://dx.doi.org/10.1016/j.advwatres.2008.10.012>.
- [8] Er V, Babadagli T, Xu Z. Pore-scale investigation of the matrix-fracture interaction during CO₂ injection in naturally fractured oil reservoirs. *Energy Fuels* 2010;24(2):1421–30. <http://dx.doi.org/10.1021/ef901038y>.
- [9] Zhang C, Oostrom M, Grate JW, Wietsma TW, Warner MG. Liquid CO₂ displacement of water in a dual-permeability pore network micromodel. *Environ Sci Technol* 2011;45(17):7581–8. <http://dx.doi.org/10.1021/es201858r>.
- [10] Wang Y, Zhang C, Wei N, Oostrom M, Wietsma TW, Li X, Bonneville A. Experimental study of crossover from capillary to viscous fingering for supercritical CO₂-water displacement in a homogeneous pore network. *Environ Sci Technol* 2013;47(1):212–8. <http://dx.doi.org/10.1021/es3014503>.
- [11] Kim M, Sell A, Sinton D. Aquifer-on-a-chip: understanding pore-scale salt precipitation dynamics during CO₂ sequestration. *Lab Chip* 2013;13:2508–18. <http://dx.doi.org/10.1039/C3LC00031A>.
- [12] Blunt M, King P. Relative permeabilities from two- and three-dimensional pore-scale network modelling. *Transp Porous Med* 1991;6(4):407–33. <http://dx.doi.org/10.1007/BF00136349>.
- [13] Bryant S, Blunt M. Prediction of relative permeability in simple porous media. *Phys Rev A* 1992;46:2004–11. <http://dx.doi.org/10.1103/PhysRevA.46.2004>.
- [14] Al-Gharbi MS, Blunt MJ. Dynamic network modeling of two-phase drainage in porous media. *Phys Rev E* 2005;71:016308. <http://dx.doi.org/10.1103/PhysRevE.71.016308>.
- [15] Valvatne P, Piri M, Lopez X, Blunt M. Predictive pore-scale modeling of single and multiphase flow. *Transp Porous Med* 2005;58:23–41. <http://dx.doi.org/10.1007/s11242-004-5468-2>.
- [16] Piri M, Blunt MJ. Three-dimensional mixed-wet random pore-scale network modeling of two- and three-phase flow in porous media. I. Model description. *Phys Rev E* 2005;71:026301. <http://dx.doi.org/10.1103/PhysRevE.71.026301>.
- [17] Blunt MJ, Bijeljic B, Dong H, Gharbi O, Iglesias S, Mostaghimi P, Paluszny A, Penland C. Pore-scale imaging and modelling. *Adv Water Resour* 2013;51:197–216. <http://dx.doi.org/10.1016/j.advwatres.2012.03.003>.
- [18] Pan C, Hilpert M, Miller C. Lattice-Boltzmann simulation of two-phase flow in porous media. *Water Resour Res* 2004;40:W01501. <http://dx.doi.org/10.1029/2003WR002120>.

- [19] Li H, Pan C, Miller CT. Pore-scale investigation of viscous coupling effects for two-phase flow in porous media. *Phys Rev E* 2005;72:026705. <http://dx.doi.org/10.1103/PhysRevE.72.026705>.
- [20] Ahrenholz B, Tölke J, Lehmann P, Peters A, Kaestner A, Krafczyk M, Durner W. Prediction of capillary hysteresis in a porous material using lattice-Boltzmann methods and comparison to experimental data and a morphological pore network model. *Adv Water Resour* 2008;31(9):1151–73. <http://dx.doi.org/10.1016/j.advwatres.2008.03.009>.
- [21] Porter M, Schaap M, Wildenschild D. Lattice-Boltzmann simulations of the capillary pressure-saturation-interfacial area relationship for porous media. *Adv Water Resour* 2009;32(11):1632–40. <http://dx.doi.org/10.1016/j.advwatres.2009.08.009>.
- [22] Hao L, Ping. Lattice Boltzmann simulations of water transport in gas diffusion layer of a polymer electrolyte membrane fuel cell. *J Power Sources* 2010;195:3870–81. <http://dx.doi.org/10.1016/j.jpowsour.2009.11.125>.
- [23] Liu H, Valocchi AJ, Kang Q, Werth C. Pore-scale simulations of gas displacing liquid in a homogeneous pore network using the lattice Boltzmann method. *Transp Porous Med* 2013;99:555–80. <http://dx.doi.org/10.1007/s11242-013-0200-8>.
- [24] Tartakovsky AM, Meakin P. Pore scale modeling of immiscible and miscible fluid flows using smoothed particle hydrodynamics. *Adv Water Resour* 2006;29:1464–78. <http://dx.doi.org/10.1016/j.advwatres.2005.11.014>.
- [25] Tartakovsky AM, Ward AL, Meakin P. Pore-scale simulations of drainage of heterogeneous and anisotropic porous media. *Phys Fluids* 2007;19:103301. <http://dx.doi.org/10.1063/1.2772529>.
- [26] Gouet-Kaplan M, Tartakovsky A, Berkowitz B. Simulation of the interplay between resident and infiltrating water in partially saturated porous media. *Water Resour Res* 2009;45:W05416. <http://dx.doi.org/10.1029/2008WR007350>.
- [27] Bandara UC, Tartakovsky AM, Palmer BJ. Pore-scale study of capillary trapping mechanism during CO₂ injection in geological formations. *Int J Greenhouse Gas Control* 2011;5:1566–77. <http://dx.doi.org/10.1016/j.ijgcc.2011.08.014>.
- [28] Huang H, Meakin P, Liu M. Computer simulation of two-phase immiscible fluid motion in unsaturated complex fractures using a volume of fluid method. *Water Resour Res* 2005;41(12):W12413. <http://dx.doi.org/10.1029/2005WR004204>.
- [29] Raeini AQ, Blunt MJ, Bijeljic B. Modelling two-phase flow in porous media at the pore scale using the volume-of-fluid method. *J Comput Phys* 2012;231:5653–68. <http://dx.doi.org/10.1016/j.jcp.2012.04.011>.
- [30] Ferrari A, Lunati I. Direct numerical simulations of interface dynamics to link capillary pressure and total surface energy. *Adv Water Resour* 2013;57:19–31. <http://dx.doi.org/10.1016/j.advwatres.2013.03.005>.
- [31] Prodanović M, Bryant S. A level set method for determining critical curvatures for drainage and imbibition. *J Colloid Interface Sci* 2006;304(2):442–58. <http://dx.doi.org/10.1016/j.jcis.2006.08.048>.
- [32] Jettestuen E, Helland JO, Prodanović M. A level set method for simulating capillary-controlled displacements at the pore scale with nonzero contact angles. *Water Resour Res* 2013;49(8):4645–61. <http://dx.doi.org/10.1002/wrcr.20334>.
- [33] Shyy W, Smith RW, Udaykumar HS, Rao MM. Computational fluid dynamics with moving boundaries. Washington, DC: Taylor & Francis; 1996.
- [34] Zhou G, Ge W, Li J. Theoretical analysis on the applicability of traditional SPH method. *Chin Sci Bull* 2013;58:2970–8. <http://dx.doi.org/10.1007/s11434-013-5889-9>.
- [35] Aidun CK, Clausen JR. Lattice-Boltzmann method for complex flows. *Annu Rev Fluid Mech* 2010;42(1):439–72. <http://dx.doi.org/10.1146/annurev-fluid-121108-145519>.
- [36] Liu H, Zhang Y. Phase-field modeling droplet dynamics with soluble surfactants. *J Comput Phys* 2010;229(4):9166–87. <http://dx.doi.org/10.1016/j.jcp.2010.08.031>.
- [37] Parmigiani A, Huber C, Bachmann O, Chopard B. Pore-scale mass and reactant transport in multiphase porous media flows. *J Fluid Mech* 2011;686:40–76. <http://dx.doi.org/10.1017/jfm.2011.268>.
- [38] Liu H, Zhang Y, Valocchi AJ. Modeling and simulation of thermocapillary flows using lattice Boltzmann method. *J Comput Phys* 2012;231(12):4433–53. <http://dx.doi.org/10.1016/j.jcp.2012.02.015>.
- [39] Chen L, Kang Q, Robinson BA, He Y-L, Tao W-Q. Pore-scale modeling of multiphase reactive transport with phase transitions and dissolution-precipitation processes in closed systems. *Phys Rev E* 2013;87:043306. <http://dx.doi.org/10.1103/PhysRevE.87.043306>.
- [40] Chen S, Doolen GD. Lattice Boltzmann method for fluid flows. *Annu Rev Fluid Mech* 1998;30(1):329–64. <http://dx.doi.org/10.1146/annurev.fluid.30.1.329>.
- [41] Gunstensen AK, Rothman DH, Zaleski S, Zanetti G. Lattice Boltzmann model of immiscible fluids. *Phys Rev A* 1991;43(8):4320–7. <http://dx.doi.org/10.1103/PhysRevA.43.4320>.
- [42] Reis T, Phillips TN. Lattice Boltzmann model for simulating immiscible two-phase flows. *J Phys A Math Theor* 2007;40(14):4033–53. <http://dx.doi.org/10.1088/1751-8113/40/14/018>.
- [43] Shan X, Chen H. Lattice Boltzmann model for simulating flows with multiple phases and components. *Phys Rev E* 1993;47(3):1815–9. <http://dx.doi.org/10.1103/PhysRevE.47.1815>.
- [44] Shan X, Chen H. Simulation of nonideal gases and liquid-gas phase transitions by the lattice Boltzmann equation. *Phys Rev E* 1994;49:2941. <http://dx.doi.org/10.1103/PhysRevE.49.2941>.
- [45] Shan X, Doolen G. Multicomponent lattice-Boltzmann model with interparticle interaction. *J Stat Phys* 1995;81:379–93. <http://dx.doi.org/10.1007/BF02179985>.
- [46] Swift MR, Osborn WR, Yeomans JM. Lattice Boltzmann simulation of nonideal fluids. *Phys Rev Lett* 1995;75(5):830–3. <http://dx.doi.org/10.1103/PhysRevLett.75.830>.
- [47] Swift MR, Orlandini E, Osborn WR, Yeomans JM. Lattice Boltzmann simulations of liquid-gas and binary fluid systems. *Phys Rev E* 1996;54(5):5041–52. <http://dx.doi.org/10.1103/PhysRevE.54.5041>.
- [48] He X, Chen S, Zhang R. A lattice Boltzmann scheme for incompressible multiphase flow and its application in simulation of Rayleigh-Taylor instability. *J Comput Phys* 1999;152(2):642–63. <http://dx.doi.org/10.1006/jcph.1999.6257>.
- [49] Sukop MC, Or D. Lattice Boltzmann method for modeling liquid-vapor interface configurations in porous media. *Water Resour Res* 2004;40:W01509. <http://dx.doi.org/10.1029/2003WR002333>.
- [50] Ghassemi A, Pak A. Numerical study of factors influencing relative permeabilities of two immiscible fluids flowing through porous media using lattice Boltzmann method. *J Pet Sci Eng* 2011;77(1):135–45. <http://dx.doi.org/10.1016/j.petrol.2011.02.007>.
- [51] Huang H, Lu X-Y. Relative permeabilities and coupling effects in steady-state gas-liquid flow in porous media: a lattice Boltzmann study. *Phys Fluids* 2009;21:092104. <http://dx.doi.org/10.1063/1.3225144>.
- [52] Dou Z, Zhou Z-F. Numerical study of non-uniqueness of the factors influencing relative permeability in heterogeneous porous media by lattice Boltzmann method. *Int J Heat Fluid Flow* 2013;42:23–32. <http://dx.doi.org/10.1016/j.ijheatfluidflow.2013.01.020>.
- [53] Dong B, Yan YY, Li WZ. LBM simulation of viscous fingering phenomenon in immiscible displacement of two fluids in porous media. *Transp Porous Med* 2011;88(2):293–314. <http://dx.doi.org/10.1007/s11242-011-9740-y>.
- [54] Yu Z, Yang H, Fan L-S. Numerical simulation of bubble interactions using an adaptive lattice Boltzmann method. *Chem Eng Sci* 2011;66:3441–51. <http://dx.doi.org/10.1016/j.ces.2011.01.019>.
- [55] Porter ML, Coon ET, Kang Q, Moulton JD, Carey JW. Multicomponent interparticle-potential lattice Boltzmann model for fluids with large viscosity ratios. *Phys Rev E* 2012;86:036701. <http://dx.doi.org/10.1103/PhysRevE.86.036701>.
- [56] Bao J, Schaefer L. Lattice boltzmann equation model for multi-component multi-phase flow with high density ratios. *Appl Math Model* 2013;37(4):1860–71. <http://dx.doi.org/10.1016/j.apm.2012.04.048>.
- [57] Nourgaliev RR, Dinh TN, Theofanous TG, Joseph D. The lattice Boltzmann equation method: theoretical interpretation, numerics and implications. *Int J Multiphase Flow* 2003;29(1):117–69. [http://dx.doi.org/10.1016/S0301-9322\(02\)00108-8](http://dx.doi.org/10.1016/S0301-9322(02)00108-8).
- [58] Liu H, Valocchi AJ, Kang Q. Three-dimensional lattice Boltzmann model for immiscible two-phase flow simulations. *Phys Rev E* 2012;85:046309. <http://dx.doi.org/10.1103/PhysRevE.85.046309>.
- [59] Suekane T, Soukawa S, Iwatai S, Tsushima S, Hirai S. Behavior of supercritical CO₂ injected into porous media containing water. *Energy* 2005;30:2370–82. <http://dx.doi.org/10.1016/j.energy.2005.10.026>.
- [60] Perrin J-C, Krause M, Kuo C-W, Miljkovic L, Charoba E, Benson SM. Core-scale experimental study of relative permeability properties of CO₂ and brine in reservoir rocks. *Energy Procedia* 2009;1(1):3515–22. <http://dx.doi.org/10.1016/j.egypro.2009.02.144>.
- [61] Perrin J-C, Benson S. An experimental study on the influence of sub-core scale heterogeneities on CO₂ distribution in reservoir rocks. *Transp Porous Med* 2010;82:93–109. <http://dx.doi.org/10.1007/s11242-009-9426-x>.
- [62] Shi J-Q, Xue Z, Durukan S. Supercritical CO₂ core flooding and imbibition in Tako sandstone-influence of sub-core scale heterogeneity. *Int J Greenhouse Gas Control* 2011;5(1):75–87. <http://dx.doi.org/10.1016/j.ijgcc.2010.07.003>.
- [63] Qian YH, D'Humières D, Lallemand P. Lattice BGK models for Navier-Stokes equation. *Europhys Lett* 1992;17:479–84. <http://dx.doi.org/10.1209/0295-5075/17/6/001>.
- [64] Zhang C, Oostrom M, Wietsma T, Grate J, Warner M. Influence of viscous and capillary forces on immiscible fluid displacement: pore-scale experimental study in a water-wet micromodel demonstrating viscous and capillary fingering. *Energy Fuels* 2011;25(8):3493–505. <http://dx.doi.org/10.1021/ef101732k>.
- [65] He X, Zou Q, Luo L-S, Dembo M. Analytic solutions of simple flows and analysis of nonslip boundary conditions for the lattice Boltzmann BGK model. *J Stat Phys* 1997;87:115–36. <http://dx.doi.org/10.1007/BF02181482>.
- [66] Ginzburg I, Adler PM. Surface tension models with different viscosities. *Transp Porous Med* 1995;20:37–76. <http://dx.doi.org/10.1007/BF00616925>.
- [67] Ginzburg I, Steiner K. A free surface lattice Boltzmann method for modelling the filling of expanding cavities by Bingham fluids. *Philos Trans R Soc Lond A* 2002;360:453–66. <http://dx.doi.org/10.1098/rsta.2001.0941>.
- [68] d'Humières D, Ginzburg I, Krafczyk M, Lallemand P, Luo L-S. Multiple-relaxation-time lattice Boltzmann models in three dimensions. *Philos Trans R Soc A* 2002;360:437–51. <http://dx.doi.org/10.1098/rsta.2001.0955>.
- [69] Pooley CM, Furtado K. Eliminating spurious velocities in the free-energy lattice Boltzmann method. *Phys Rev E* 2008;77:046702. <http://dx.doi.org/10.1103/PhysRevE.77.046702>.
- [70] Yu Z, Fan L-S. Multirelaxation-time interaction-potential-based lattice Boltzmann model for two-phase flow. *Phys Rev E* 2010;82:046708. <http://dx.doi.org/10.1103/PhysRevE.82.046708>.

- [71] Liu H, Valocchi AJ, Zhang Y, Kang Q. Lattice Boltzmann phase-field modeling of thermocapillary flows in a confined microchannel. *J Comput Phys* 2014;256:334–56. <http://dx.doi.org/10.1016/j.jcp.2013.08.054>.
- [72] Zu YQ, He S. Phase-field-based lattice Boltzmann model for incompressible binary fluid systems with density and viscosity contrasts. *Phys Rev E* 2013;87:043301. <http://dx.doi.org/10.1103/PhysRevE.87.043301>.
- [73] Coward AV, Renardy YY, Renardy M, Richards JR. Temporal evolution of periodic disturbances in two-layer Couette flow. *J Comput Phys* 1997;132:346–61. <http://dx.doi.org/10.1006/jcph.1996.5640>.
- [74] Ginzburg I. Lattice Boltzmann modeling with discontinuous collision components: hydrodynamic and advection-diffusion equations. *J Stat Phys* 2007;126:157–206. <http://dx.doi.org/10.1007/s10955-006-9234-4>.
- [75] Tölke J. Lattice Boltzmann simulations of binary fluid flow through porous media. *Philos Trans R Soc Lond A* 2002;360:535–45. <http://dx.doi.org/10.1098/rsta.2001.0944>.
- [76] Liu H, Zhang Y. Droplet formation in microfluidic cross-junctions. *Phys Fluids* 2011;23:082101. <http://dx.doi.org/10.1063/1.3615643>.
- [77] Aursjø O, Løvoll G, Knudsen HA, Flekkøy EG, Máloy KJ. A direct comparison between a slow pore scale drainage experiment and a 2d lattice Boltzmann simulation. *Transp Porous Med* 2011;86:125–34. <http://dx.doi.org/10.1007/s11242-010-9611-y>.
- [78] Tölke J, Prisco GD, Mu Y. A lattice Boltzmann method for immiscible two-phase Stokes flow with a local collision operator. *Comput Math Appl* 2013;65:864–81. <http://dx.doi.org/10.1016/j.camwa.2012.05.018>.
- [79] Grunau D, Chen S, Eggert K. A lattice Boltzmann model for multiphase fluid flows. *Phys Fluids A* 1993;5:2557. <http://dx.doi.org/10.1063/1.858769>.
- [80] Latva-Kokko M, Rothman DH. Diffusion properties of gradient-based lattice Boltzmann models of immiscible fluids. *Phys Rev E* 2005;71:056702. <http://dx.doi.org/10.1103/PhysRevE.71.056702>.
- [81] Leclaire S, Reggio M, Trépanier J-Y. Numerical evaluation of two recoloring operators for an immiscible two-phase flow lattice Boltzmann model. *Appl Math Model* 2012;36:2237–52. <http://dx.doi.org/10.1016/j.apm.2011.08.027>.
- [82] Halliday I, Hollis AP, Care CM. Lattice Boltzmann algorithm for continuum multicomponent flow. *Phys Rev E* 2007;76:026708. <http://dx.doi.org/10.1103/PhysRevE.76.026708>.
- [83] Ladd AJC. Numerical simulations of particulate suspensions via a discretized Boltzmann equation (Part I & II). *J Fluid Mech* 1994;271:285–339. <http://dx.doi.org/10.1017/S0022112094001783>.
- [84] Rowlinson JS, Widom B. *Molecular theory of capillarity*. London: Clarendon Press; 1989.
- [85] Bekri S, Adler PM. Dispersion in multiphase flow through porous media. *Int J Multiphase Flow* 2002;28(4):665–97. [http://dx.doi.org/10.1016/S0301-9322\(01\)00089-1](http://dx.doi.org/10.1016/S0301-9322(01)00089-1).
- [86] van der Graaf S, Nisisako T, Schroën CGPH, van der Sman RGM, Boom RM. Lattice Boltzmann simulations of droplet formation in a T-shaped microchannel. *Langmuir* 2006;22:4144–52. <http://dx.doi.org/10.1021/la052682f>.
- [87] Liu H, Zhang Y. Droplet formation in a T-shaped microfluidic junction. *J Appl Phys* 2009;106:034906. <http://dx.doi.org/10.1063/1.3187831>.
- [88] Liu H, Zhang Y. Lattice Boltzmann simulation of droplet generation in a microfluidic cross-junction. *Commun Comput Phys* 2011;9:1235–56. <http://dx.doi.org/10.4208/cicp.231009.101110s>.
- [89] Marty S, Chen H. Simulation of multicomponent fluids in complex three-dimensional geometries by the lattice Boltzmann method. *Phys Rev E* 1996;53:743–50. <http://dx.doi.org/10.1103/PhysRevE.53.743>.
- [90] Yiotis AG, Psihogios J, Kainourgiakis ME, Papaioannou A, Stubos AK. A lattice Boltzmann study of viscous coupling effects in immiscible two-phase flow in porous media. *Colloid Surf A – Physicochem Eng Asp* 2007;300:35–49. <http://dx.doi.org/10.1016/j.colsurfa.2006.12.045>.
- [91] Briant AJ, Yeomans JM. Lattice Boltzmann simulations of contact line motion. II. Binary fluids. *Phys Rev E* 2004;69:031603. <http://dx.doi.org/10.1103/PhysRevE.69.031603>.
- [92] Washburn EW. The dynamics of capillary flow. *Phys Rev* 1921;17:273–83. <http://dx.doi.org/10.1103/PhysRev.17.273>.
- [93] Diotallevi F, Biferale L, Chibbaro S, Lamura A, Pontrelli G, Sbragaglia M, Succi S, Toschi F. Capillary filling using lattice Boltzmann equations: the case of multi-phase flows. *Eur Phys J Spec Top* 2009;166:111–6. <http://dx.doi.org/10.1140/epj/e/2009-00889-7>.
- [94] Pooley C, Kusumaatmaja H, Yeomans J. Modelling capillary filling dynamics using lattice Boltzmann simulations. *Eur Phys J Spec Top* 2009;171(1):63–71. <http://dx.doi.org/10.1140/epj/e/2009-01012-0>.
- [95] Lenormand R, Toublou E, Zarcone C. Numerical models and experiments on immiscible displacements in porous media. *J Fluid Mech* 1988;189:165–87. <http://dx.doi.org/10.1017/S0022112088000953>.
- [96] Ginzburg I, d'Humières D. Multireflection boundary conditions for lattice Boltzmann models. *Phys Rev E* 2003;68:066614. <http://dx.doi.org/10.1103/PhysRevE.68.066614>.
- [97] Pan C, Luo L-S, Miller CT. An evaluation of lattice Boltzmann schemes for porous medium flow simulation. *Comput Fluids* 2006;35:898–909. <http://dx.doi.org/10.1016/j.compfluid.2005.03.008>.
- [98] d'Humières D, Ginzburg I. Viscosity independent numerical errors for lattice Boltzmann models: from recurrence equations to magic collision numbers. *Comput Math Appl* 2009;58(5):823–40. <http://dx.doi.org/10.1016/j.camwa.2009.02.008>.
- [99] Talon L, Bauer D, Gland N, Youssef S, Auradou H, Ginzburg I. Assessment of the two relaxation time lattice Boltzmann scheme to simulate Stokes flow in porous media. *Water Resour Res* 2012;48:W04526. <http://dx.doi.org/10.1029/2011WR011385>.
- [100] Hao L, Cheng P. Lattice Boltzmann simulations of anisotropic permeabilities in carbon paper gas diffusion layers. *J Power Sources* 2009;186:104–14. <http://dx.doi.org/10.1016/j.jpowsour.2008.09.086>.
- [101] Moqtaderi H, Esfahanian V. Evaluation of a new solid boundary implementation in the lattice Boltzmann method for porous media considering permeability and apparent slip. *Philos Trans R Soc A* 2011;369:2193–201. <http://dx.doi.org/10.1098/rsta.2011.0095>.
- [102] Gao Y, Rama P, Ostdadi H, Jiang K, Chen R, Zhang X. An improved MRT lattice Boltzmann model for calculating anisotropic permeability of compressed and uncomressed carbon cloth gas diffusion layers based on X-ray computed micro-tomography. *J Fuel Cell Sci Technol* 2012;9:041010. <http://dx.doi.org/10.1115/1.4006796>.
- [103] Genty A, Pot V. Numerical simulation of 3D liquid-gas distribution in porous media by a two-phase TRT lattice Boltzmann method. *Transp Porous Med* 2013;96:271–94. <http://dx.doi.org/10.1007/s11242-012-0087-9>.
- [104] Zhang Y-H, Gu X-J, Barber RW, Emerson DR. Capturing Knudsen layer phenomena using a lattice Boltzmann model. *Phys Rev E* 2006;74:046704. <http://dx.doi.org/10.1103/PhysRevE.74.046704>.